Heliyon 11 (2025) e44010

Contents lists available at ScienceDirect

Heliyon

journal homepage: www.cell.com/heliyon

Research article

Characterization of astrocytic primary cilia in the adult mouse cortex and hippocampus

Sylvie C. Lahaie [a,b], Albert HK. Fok [a], Jessica M. Nicholls [a], Hannah Lee [a], Tabish A. Syed [a], Sabrina Chierzi [a], Sayuri Hatada [e], Naomi Egawa [e], Alex L. Schober [a,b], Tak Yi Mayumi Wong [a,b], Robert Royston Jr. [a], Kaleem Siddiqi [c,d], Yoshiyuki Kubota [e,f,g], Keith K. Murai [a,b,h,*]

[a] Centre for Research in Neuroscience, Department of Neurology & Neurosurgery, Brain Repair and Integrative Neuroscience Program, The Research Institute of the McGill University Health Centre, Montreal General Hospital, 1650 Cedar Avenue, Montreal, QC, H3G 1A4, Canada
[b] Integrated Program in Neuroscience, McGill University, Montreal, Quebec, Canada
[c] School of Computer Science and Centre for Intelligent Machines, McGill University, 3480 Rue University, Montreal, QC, H3A 2A7, Canada
[d] MILA - Québec AI Institute, 6666 Rue Saint-Urbain, Montreal, QC, H2S 3H1, Canada
[e] Section of Electron Microscopy, Supportive Center for Brain Research, National Institute for Physiological Sciences (NIPS), Okazaki, 444-8787, Japan
[f] The Graduate University for Advanced Studies (SOKENDAI), Okazaki, 444-8787, Japan
[g] Support Unit for Electron Microscopy Techniques, Research Resources Division, RIKEN Center for Brain Science, Wako, 351-0198, Japan
[h] School of Biomedical Sciences, McGill University, 3649 Promenade Sir-William Osler, Montreal, QC, H3G 0B1, Canada

ARTICLE INFO

Keywords:
Astrocyte
Neuron
Cilia
Confocal imaging
Electron microscopy
Cortex
Hippocampus

ABSTRACT

The primary cilium is a single, antenna-like projection found on the surface of eukaryotic cells. Primary cilia contain cell signaling components that are critical for developmental patterning and cell cycle maintenance. New functions for primary cilia are being discovered in the context of the central nervous system (CNS) and neurological diseases. Yet, the fundamental properties of primary cilia on cells in the CNS remain to be fully understood. This is especially true for astrocytes, an abundant CNS cell type that has key roles in CNS development, function, homeostasis, and response to disease. In this study, we analyze astrocytic primary cilia using a combination of light and serial electron microscopy approaches in the hippocampus and the cortex in adult mice. We report distinct properties of astrocytic primary cilia in these brain regions in comparison to nearby neuronal primary cilia with respect to molecular composition, length, orientation, and local connectivity. Furthermore, we show that the properties of astrocytic and neuronal primary cilia can vary between and within hippocampal and cortical subregions/strata and this can be influenced by sex. Serial electron microscopy reveals structural diversity of the astrocytic ciliary pocket, leading to variations in extracellular exposure and local connectivity of the primary cilia. We further show that expression of a mutant primary cilia protein in astrocytes during development leads to sparse distribution of astrocytes in the upper cortical layers. Unique properties of astrocytic primary cilia may indicate their differential ability to signal in response to extracellular environmental cues to regulate the molecular and structural properties of astrocytes.

* Corresponding author. Centre for Research in Neuroscience 1650 Cedar Avenue L12Montreal, QC, H3G 1A4 Canada,
E-mail address: keith.murai@mcgill.ca (K.K. Murai).

https://doi.org/10.1016/j.heliyon.2025.e44010
Received 17 September 2024; Received in revised form 5 September 2025; Accepted 1 October 2025
Available online 3 November 2025

1. Introduction

The primary cilium is a single, antenna-like structure on the surface of many eukaryotic cells [1,2] and it contains an array of signaling receptors and proteins including Sonic hedgehog (Shh) receptors [3,4], melanocortin (MCR) receptor [5,6], serotonin receptors [7], and somatostatin receptors [8]. Their specialized double membrane, centriole-anchored [9], non-motile 9 + 0 microtubule

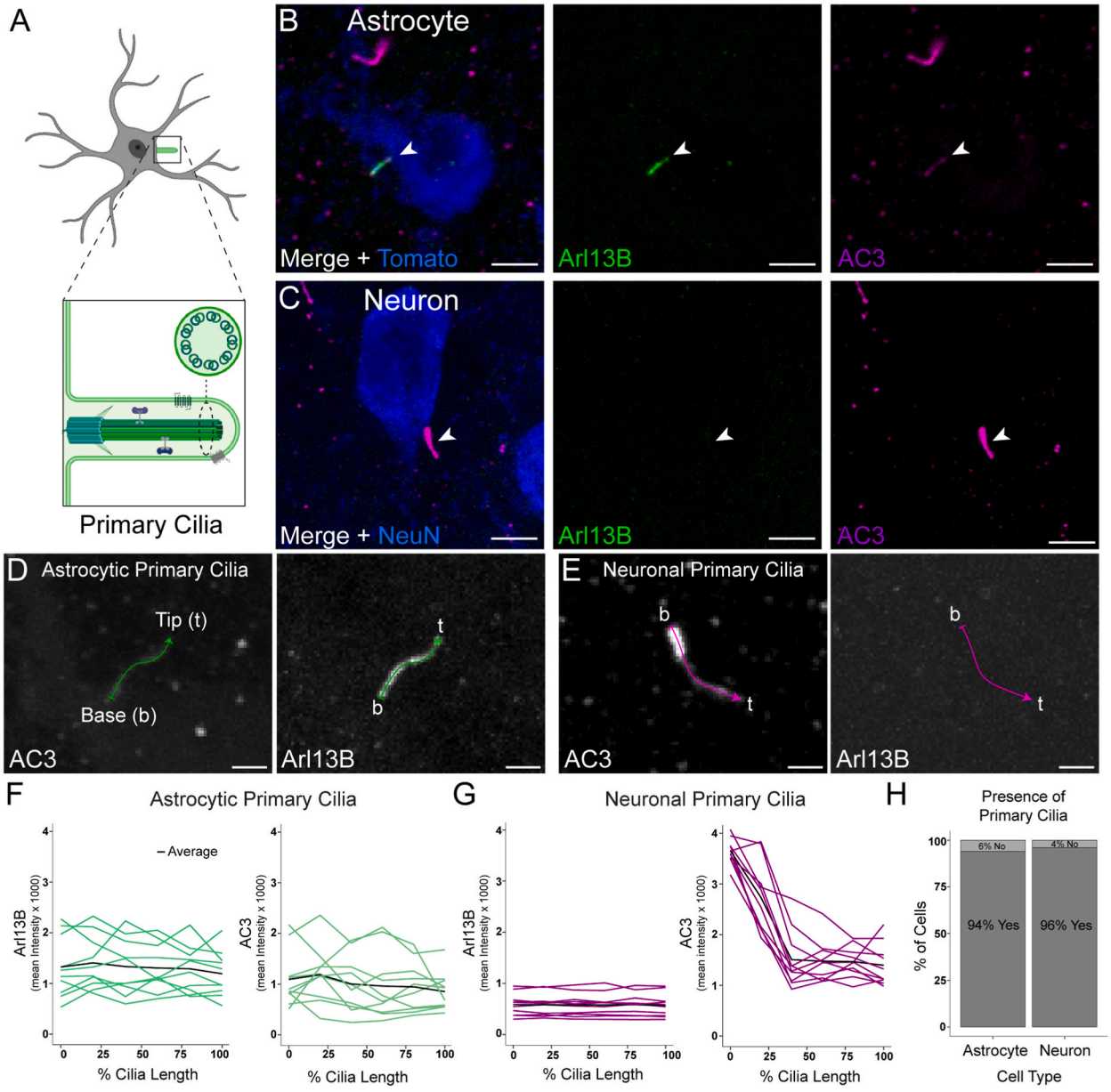

Fig. 1. Astrocytic and neuronal primary cilia labeling with primary cilia markers Arl13B and AC3. (A) Schematic of an astrocyte with a primary cilium with its molecular components, basal body base and microtubule arrangement. (B–C) Astrocytic and neuronal primary cilium labeled by Arl13B and AC3 *in vivo*, respectively. Astrocytes were identified by Tomato signal and neurons were identified by NeuN. Scale bar = 5 μm. (D) Trace of astrocytic primary cilium from cortex and hippocampus in P30 mice with both AC3 and Arl13B signal showing the path for the mean intensity measurements from base (b) to tip (t). Scale bar = 2 μm (n = 10). (E) Trace of neuronal primary cilium from cortex and hippocampus in P30 mice with both AC3 and Arl13B signal showing the path for the mean intensity measurement from base (b) to tip (t). Scale bar = 2 μm (n = 10). (F) Mean intensity graphs of Arl13B and AC3 signal for astrocytic primary cilia from base (b) to tip (t), 0 % being the base and 100 % being the tip. (G) Mean intensity graphs of Arl13B and AC3 signal for neuronal primary cilia from base (b) to tip (t), 0 % being the base and 100 % being the tip (n = 10). (H) Percentage of astrocytes and neurons that contain a primary cilium in both cortex and hippocampus in P30 mice (astrocytes n = 780, neurons n = 1228). Arl13B: ADP-ribosylation factor-like GTPase 13 B, AC3: Adenylate cyclase type III, NeuN: Neuronal nuclei. Graphics created with BioRender.com.

arrangement [10], and extension from the cell surface allows this distinctive structure to detect cues in the extracellular environment and play key roles in processes including transcriptional regulation [3,4], developmental patterning [11,12], and cycle cell regulation [13]. Mutations in genes encoding primary cilia proteins lead to a class of genetic disorders called ciliopathies [14], which often manifest in developmental conditions that impact a variety of tissues including the retina, kidney, and nervous system. Notably, however, primary cilia persist into adulthood on many cell types in the body, and hence they are in a position to regulate cell properties in mature cells and their associated tissues. Consistent with this, primary cilia have been implicated in diseases that persist or emerge in adulthood such as obesity [15,16], cancer [17,18], and neurodegeneration [19–22].

While studies have made important progress in understanding primary cilia in neurons and glial cell subtypes within the CNS [23–26], some basic organizational and structural properties of primary cilia in mature CNS cells remain to be better understood. This is especially the case for astrocytes, a major CNS cell type that plays a multi-functional role in brain development, function, plasticity, and response to injury/disease. Astrocytes are a heterogenous population of glial cells whose transcriptional program is impacted by cues derived from their microenvironment. Studies, including from our group, have previously demonstrated that astrocytes become diversified, in part, through their local response to neuron-derived Shh, thereby allowing nearby neurons to control the astrocytic genetic program [27–29]. A recent study showed that region-specific astrocytic diversity relies on Shh signaling through the primary cilium. Moreover, conditional deletion of the primary cilia molecules Arl13b or Ift88 results in transcriptional changes and morphological alterations to cortical astrocytes that impact behavior in mice [30]. Astrocytes are also highly sensitive to brain injury and cell pathology which causes astrocyte reactivity [31]. Recent studies have begun to look at the relationship between primary cilia and astrocyte reactivity, in particular investigating neuroinflammation [32,33] mitochondrial stress [34] and neurodegeneration [22] However, the role of the primary cilia in astrocytic reactivity and the transformation of molecular, structural, and functional properties of astrocytes requires further investigation [35].

In this study, we investigate the organizational and structural properties of astrocytic primary cilia using a combination of light and serial electron microscopy approaches in the healthy adult rodent nervous system. We demonstrate that astrocytic primary cilia show some dissimilarities to neuronal primary cilia and that these differences vary according to the brain region, cell positioning, and sex. Serial reconstruction of primary cilia from a volume electron microscopy (vEM) dataset further reveals the differential ultrastructure, organization, and connectivity of astrocytic primary cilia when compared to those found on neurons. *In vivo* expression of a mutant dominant negative (Arl13B T35N mutant) primary cilia protein in developing astrocytes using *in utero* electroporation alters the ability of astrocytes to be sustained in upper cortical layers [36]. The unique features of astrocytic primary cilia may enable these cells to differentially respond to extracellular cues that regulate their molecular and structural properties in the healthy and diseased/injured CNS.

2. Results

2.1. Astrocytic and neuronal primary cilia differentially label for Arl13B and AC3

The primary cilium is a single, hair-like extension from the surface of eukaryotic cells (Fig. 1A) and can be visualized by immunolabeling for primary cilia-enriched markers including ADP-ribosylation factor-like protein 13 B [37] (Arl13B) and Adenylyl Cyclase 3 [38] (AC3). Arl13B is a GTPase involved in ciliogenesis, shuttling signaling components in and out of the primary cilium [39]. AC3 is a cyclase involved in cilium elongation [40]. To compare how astrocytic and neuronal primary cilia label for these canonical markers, we performed high-resolution confocal imaging in postnatal day 30 mouse cortex and hippocampus (Fig. 1B, cortex shown). We genetically labeled astrocytes in the adult mouse brain using a mouse line containing tamoxifen-sensitive CreERT2 driven by the astrocyte-specific aldehyde dehydrogenase family 1, member L1 (Aldh1l1) promoter [41] crossed with a mouse line containing floxed-stop tdTomato in the ROSA26 locus [42] (Ai9; now referred to as Tomato). Mice were treated with tamoxifen at postnatal days 1–2 to induce Tomato expression in astrocytes throughout the CNS. This was followed by immunolabeling and confocal microscopy on tissue sections from postnatal day 30 mice (4 males and 4 females). NeuN was used to label neuronal nuclei and perinuclear cytoplasm. We observed that Arl13B strongly labeled primary cilia of Tomato-positive astrocytes. AC3 was also detected in astrocytic primary cilia, but the signal was weak (Fig. 1B). In contrast, AC3 strongly labeled neuronal primary cilia, whereas Arl13B was low to non-detectable (Fig. 1C). To better understand the signal distribution of these markers, we analyzed the mean intensity of the signal from the base to the tip of primary cilia in astrocytes and neurons in both the cortex and hippocampus (Fig. 1D–E). Astrocytic primary cilia, on average, showed detectable levels of Arl13B along the entire length of the primary cilium (Fig. 1D). Whereas, AC3 labeling showed, on average, a weak signal with intensities that varied from one astrocyte to another (Fig. 1F). Arl13B was low to undetectable on neuronal primary cilia, whereas AC3, while present throughout the length of the neuronal primary cilia, was concentrated at the base of the primary cilia with decreasing but consistently detectible expression at the tip (Fig. 1G). We also quantified the percentage of cells bearing a primary cilium and found that ~94 % of astrocytes and ~96 % of neurons showed Arl13B or AC3-positive primary cilia, respectively (Fig. 1H). No multi-ciliated cells were observed for any cells analyzed (*not shown*). Thus, Arl13B and AC3 are consistent markers for astrocytic and neuronal primary cilia, respectively, with the majority of astrocytes and neurons containing a detectable primary cilium.

2.2. Spatial analysis of astrocytic primary cilia and comparison with neuronal primary cilia in hippocampal area CA1

In hippocampal area CA1, neurons and astrocytes are positioned within specific strata that contribute to the organization of hippocampal connectivity [43]. Each of these strata has distinct neuronal populations in the stratum oriens (SO), stratum pyramidale

(SP), and stratum radiatum (SR) [44,45]. Molecular and structural differences between astrocytes within these strata have also been reported [46,47].

To determine if the general structure of astrocytic primary cilia varies in different CA1 hippocampal strata, we analyzed the length and orientation of primary cilia in the SO, SP, and SR (Fig. 2A). Astrocytes and neurons were identified by their expression of Tomato or NeuN, respectively. In all strata, astrocytic primary cilia were strongly labeled with Arl13B (Fig. 2B–D) and neuronal primary cilia with AC3 (Fig. 2E–G). We measured the length of the primary cilium from the base to the tip through confocal Z-stacks using the SNT [48] Fiji plugin in all three CA1 strata. We only considered primary cilia from cells where the soma of astrocytes or neurons was captured entirely in the confocal Z-stack volume. Across CA1 strata, astrocytic primary cilia were not significantly different in length, ranging between 3.15 and 3.67 μm (Fig. 2H) ($n = 8$, SO $= 3.67 \pm 0.52$ μm, SP $= 3.27 \pm 0.65$ μm, SR $= 3.15 \pm 0.62$ μm, $p = 0.2154$). Likewise, neuronal primary cilia lengths across SO, SP, and SR were not significantly different. Pooling astrocytic or neuronal primary cilia across strata showed that astrocytes had significantly shorter primary cilia (Fig. 2J) ($n = 24$, astrocytes $= 3.36 \pm 0.62$ μm, neurons $= 7.3 \pm 1.20$ μm, $p < 2.2e\text{-}16$). Interestingly, separating the data by sex, showed a significant difference in astrocytic primary cilia length between male and female mice in the SP (Supplemental Fig. 1A) ($n = 4$, Female SP $= 2.80 \pm 0.58$ μm, Male SP $= 3.74 \pm 0.26$ μm, $p = 0.02494$). Neuronal primary cilia did not show overall sex-specific differences in length (Supplemental Fig. 1B), ranging between 6.90 and 7.71 μm (Fig. 2I) ($n = 8$, SO $= 7.33 \pm 1.72$ μm, SP $= 6.90 \pm 0.62$ μm, SR $= 7.71 \pm 1.02$ μm, $p = 0.4116$). Thus, astrocytic primary cilia are ~50 % shorter than neuronal primary cilia. Furthermore, astrocytic primary cilia also exhibit sex differences in the SP layer with females having ~20 % shorter primary cilia when compared to males.

To better understand how astrocytic and neuronal primary cilia organize with respect to the structure of the hippocampus, we analyzed their three-dimensional orientations in each CA1 hippocampal strata using the 3D coordinates of the base and the tip of each primary cilium. In the SO, astrocytes displayed a preferential 'down' orientation pointing towards SP (Fig. 2K). Arrows in 3D scatter plot representing one primary cilium and colour gradient representing the Y value in which negative Y means pointing 'up' towards the alveus and positive Y means pointing 'down' towards the stratum lacunosum moleculare (SLM). In SP and SR, astrocytic primary cilia did not display a preferential orientation (Fig. 2L–M). In contrast, primary cilia in neurons in SP showed a preferred 'down' orientation (73 %) while neurons in SO and SR did not have a preferential orientation (Fig. 2N–P). In summary, astrocytic primary cilia in area CA1 therefore exhibit strata-specific orientation differences with SO astrocytes preferentially orienting their primary cilia towards the SP layer. This contrasts with the orientation of neuronal primary cilia in the SP layer which preferentially point 'down' and in the direction of the SLM. The spatial orientation of primary cilia in astrocytes and neurons may allow these cells to be exposed to spatially restricted environment cues and/or local contacts with other cells that regulate their molecular and functional properties.

2.3. Layer-specific analysis of astrocytic primary cilia in cortex and comparison to neuronal primary cilia

The adult cortex comprises six layers containing different neuronal cell types with unique connectivity patterns. Structurally and molecularly distinct astrocytic subpopulations have also been detected between and within these layers [49–51]. Using Tomato and NeuN to identify astrocytes and neurons, respectively, in different layers of the somatosensory cortex (Fig. 3A–B), we analyzed the length and orientation of astrocytic and neuronal primary cilia. As in the hippocampus, astrocytic primary cilia were strongly labeled with Arl13B in all the layers of the cortex (Fig. 3C–E) and neuronal primary cilia with AC3 (Fig. 3F–H). Astrocytic primary cilia ranged in length from 3.31 μm–3.71 μm with astrocytes in layer lV-VI having significantly shorter primary cilia (Fig. 3I) (layer I $= 3.68 \pm 0.31$ μm, layer II-III $= 3.71 \pm 0.32$ μm, layer IV-VI $= 3.31 \pm 0.43$ μm, $p = 0.0471$). Moreover, astrocytes exhibited a sex-specific difference in primary cilia length with layer II-III astrocytes in male mice showing significantly longer primary cilia (Supplementary Fig. 1C) (female, layer II-III $= 3.50 \pm 0.24$ μm; male, layer II-III $= 3.92 \pm 0.23$ μm, $p = 0.043$). Neuronal primary cilia ranged in length from 5.64 to 7.94 μm with layer l primary cilia being significantly longer (Fig. 3J) (layer I $= 7.94 \pm 1.20$ μm, layer II-III $= 5.77 \pm 0.47$ μm, layer IV-VI $= 5.64 \pm 0.35$ μm, p (top) $= 4.41e\text{-}07$, p (bottom) $= 1.81e\text{-}07$) with no detectable differences between the sexes (Supplemental Fig. 1D). Pooling astrocytes and neurons across cortical layers revealed that astrocytes had significantly shorter primary cilia than neurons (Fig. 3K) ($n = 24$, astrocytes $= 3.57 \pm 0.40$ μm, neurons $= 6.45 \pm 1.22$ μm, p value $= 1.821e\text{-}14$). Overall, astrocytic and neuronal primary cilia displayed layer specific differences in the somatosensory cortex, with astrocytic primary cilia having ~40 % shorter primary cilia than neuronal primary cilia. Interestingly, astrocytic primary cilia in layers II-III exhibited sex differences in which females have ~10 % shorter primary cilia compared to males, a similar observation made for astrocytic primary cilia in hippocampal CA1 SP (Supplemental Fig. 1A). We also analyzed primary cilia orientation in the somatosensory cortex. In all cortical layers, astrocytic primary cilia displayed no major orientation preference (Fig. 3L–N). While neuronal primary cilia in layer I did not display an orientation preference (Fig. 3O), neurons in layers II-VI preferentially oriented 'up' and towards the pial surface (Fig. 3P–Q). Overall, we show that cell type, sex, and cortical layer positioning were associated with differences in primary cilia length and orientation in astrocytes and neurons.

2.4. Ultrastructural analysis of astrocytic and neuronal primary cilia in adult rat cortex

While confocal microscopy is useful for analyzing the general structure and organization of primary cilia in the brain especially across large populations of cells, it lacks the resolution to fully appreciate the ultrastructure of the primary cilium and its intricate connections to other cells and structures in the local microenvironment. Recent studies have resolved primary cilia using vEM techniques in tissues such as the mouse visual cortex [23], mouse optic nerve [25] and human temporal cortex [24]. To better resolve the structural organization of astrocytic and neuronal primary cilia, we utilized a vEM dataset of rat motor cortex (layer V-VI) produced from an automatic tape-collecting ultra-microtome–serial electron microscopy technique (ATUM-SEM) [52]. The advantage of this

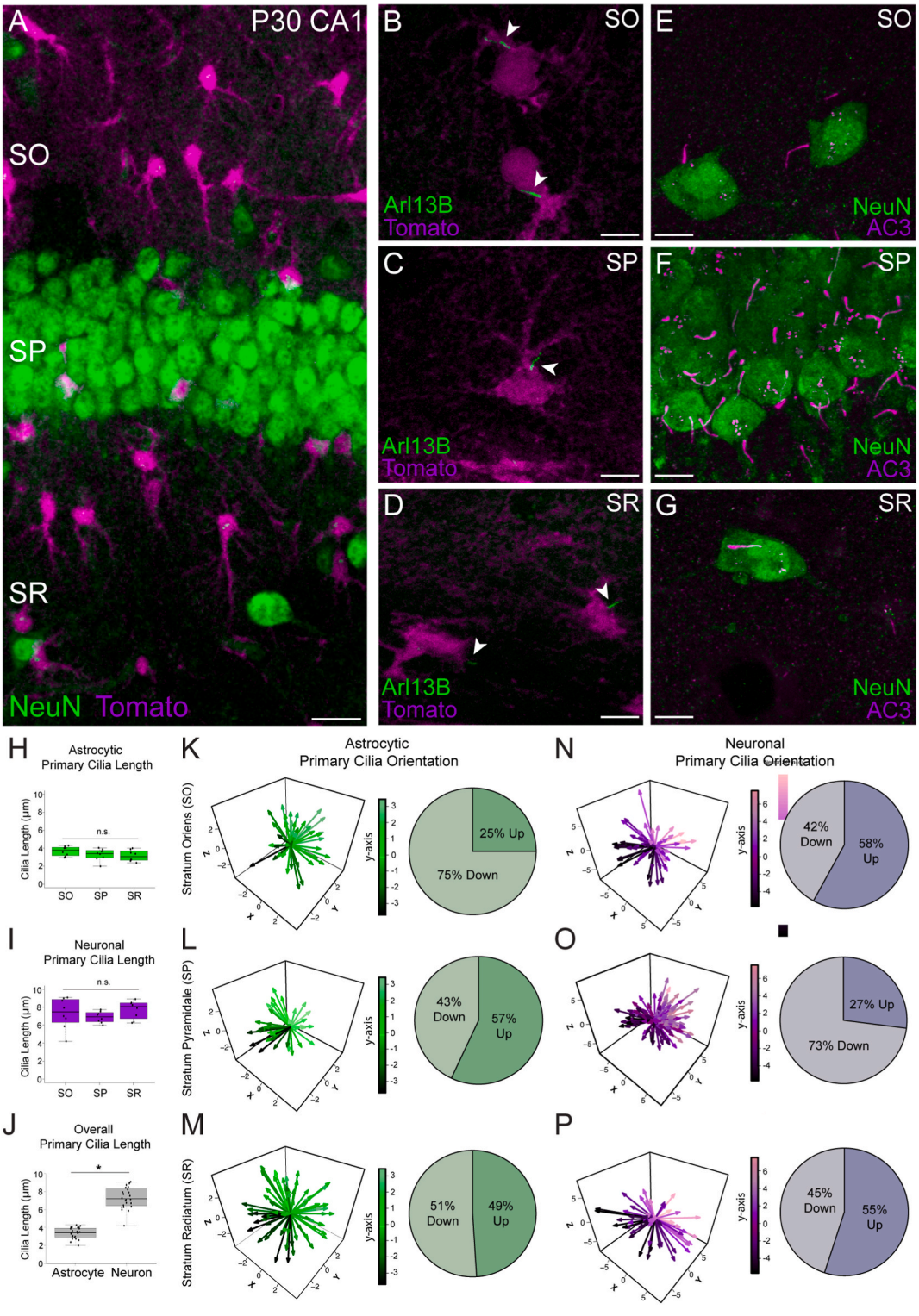

(caption on next page)

Fig. 2. Astrocytic and neuronal primary cilia in area CA1 of hippocampus at postnatal day 30. (A) Strata of CA1 hippocampus in Aldh1L1-CreERT2-tdTomato mice with NeuN labeling. Scale bar = 30 μm. Astrocyte primary cilia labeled with Arl13B in SO (B), SP (C) and SR (D). Scale bar = 5 μm. Neuronal primary cilia labeled with AC3 in SO (E), SP (F) and SR (G). Scale bar = 5 μm. (H) Astrocytic primary cilia length measurements in SO, SP and SR (n = 8, SO = 9–14 cells/animal, SP = 7–18 cells/animal, SR = 12–30 cells/animal, 3–6 sections/animal, p = 0.2154). (I) Neuronal primary cilia length measurements in SO, SP and SR (n = 8, SO = 9–18 cells/animal, SP = 21–29 cells/animal, SR = 8–20 cells/animal, 3–6 sections/animal, p = 0.4116). (J) Astrocytic and neuronal primary cilia length measurements in all regions of CA1 hippocampus (n = 8, p < 2.2e-16). Orientation of astrocytic primary cilia in SO (K), SP (L) and SR (M) (n = 4, SO = 9–14 cells/animal, PC = 7–18 cells/animal, SR = 12–30 cells/animal, 3–6 sections/animal). Orientation of neuronal primary cilia in SO (N), SP (O) and SR (P) (n = 4, SO = 11–16 cells/animal, SP = 21–29 cells/animal, SR = 9–20 cells/animal, 3–6 sections/animal). Arl13B: ADP-ribosylation factor-like GTPase 13 B, AC3: Adenylate cyclase type III, NeuN: Neuronal nuclei, SO: Stratum Oriens, tdTom: tdTomato, SP: Stratum Pyramidal, SR: Stratum Radiatum, Aldh1L1: Aldehyde dehydrogenase 1 Family Member L1. Statical tests used were Student's t-test and ANOVA.

ATUM-SEM dataset is that it allowed us to identify the soma and primary cilia of numerous astrocytes and neurons within the same volume, thereby enabling quantitative analysis of their structure. We identified and traced sixteen astrocytic primary cilia and nine neuronal primary cilia (Fig. 4D). By measuring their length in three-dimensional space, we found that, similar to light microscopy, astrocytic primary cilia are significantly shorter than neuronal primary cilia (Fig. 4E) (n = 16, Astrocyte = 2.731 ± 0.617 μm, n = 9, Neuron = 6.696 ± 1.511 μm, p value = 2.859e-09). These length measurements differ from a recent vEM study that investigated the mouse visual cortex [23], in which average astrocyte primary cilia length was approximately 7 μm. In some instances, we identified primary cilia in the longitudinal plane (Fig. 4A–B) that allowed visualization of long microtubule structures, or the axial plane, which showed the 9 + 0 microtubule assembly [10] (Fig. 4C). In many cases, we observed that the entire length of the astrocytic primary cilia was in close proximity to the astrocytic soma. This was different from neuronal primary cilia which commonly extended away from the soma *(not shown)*. Ultrastructural analysis revealed a thinning from base to tip that was observed in both astrocytic primary cilia (Fig. 4F) (n = 16, astrocyte base = 475.9 ± 77.1 nm, astrocyte middle = 323.7 ± 71.5 nm, astrocyte tip = 163.7 ± 66.2 nm) and neuronal primary cilia (Fig. 4G) (n = 9, neuron base = 462.9 ± 86.9 nm, neuron middle = 366.4 ± 139.2 nm, Neuron tip = 161.5778 ± 47.48944 nm). This thinning has been previously observed [23,24]. Most surprising, a majority of astrocytic primary cilia (56 %) were associated with a pronounced ciliary pocket (Fig. 4H), a structure which has been described in various cells from different species [23–25]. In some cases, the ciliary pocket covered a small portion of the base of the astrocytic primary cilia (Fig. 4I), allowing contact with structures such as connections with myelinated axons (Fig. 4H and Supp Fig. 2A–B), while in other cases, a large portion of the primary cilia was retained in the ciliary pocket and created a tunnel structure along the astrocyte soma (Fig. 4J).

Thus, primary cilia from cortical astrocytes and neurons displayed distinct ultrastructural features with respect to their length and organization, with astrocytic primary cilia often concealed within a ciliary pocket. This organization of astrocytic primary cilia is predicted to impact their ability to interact with the extracellular environment and regulate their exposure to cues in the interstitial space.

2.5. Perturbation of primary cilia signaling in developing astrocytes impacts astrocytic abundancy in upper cortical layers

A recent paper using gene loss-of-function and single-cell transcriptomics showed that astrocytic primary cilia signaling modulates astrocyte subtype diversity, intracellular signaling, metabolism, and morphology [30]. To further understand the basic functions of astrocytic primary cilia in cortex, we impaired the function of the astrocytic primary cilia during early astrocyte development using *in utero* electroporation by introducing a construct that causes miRNA-mediated knock down of endogenous Arl13B expression followed by replacement by either a control (WT Arl13 B-GFP) or mutant primary cilia protein (Arl13 B-T35N-GFP). The WT Arl13 B-GFP gene contained a silent mutation conferring insensitivity to miRNA-mediated knock-down. The Arl13 B-T35N-GFP gene contained the silent mutation in addition to a T35N mutation that blocks Arl13B GTPase activity thereby inhibiting primary cilia signaling [36]. We first validated the ability of the miRNA sequence against Arl13B to knockdown Arl13B protein and showed approximately 52 % knockdown efficiency of miRNA sensitive Arl13 B-GFP (Fig. 5A–C) (n = 6, control = 462.9545 ± 53.95624, Arl13B miRNA = 241.4317 ± 15.01285, p-value = 2.123e-06). To knockdown Arl13B expression and drive expression of control Arl13 B-GFP or mutant Arl13 B-T35N-GFP in astrocytes *in vivo*, we designed a PiggyBac transposon approach to knockdown endogenous Arl13B, and to replace it with either miRNA-insensitive control Arl13 B-GFP or mutant Arl13 B-T35N-GFP, all under the hGfaABC1D promoter [53] (Fig. 5D). Each of these constructs was co-electroporated at E16.5 with a plasmid to express membrane-targeted mCherry in astrocytes [54]. This led to efficient expression of control Arl13 B-GFP or Arl13 B-T35N-GFP proteins in astrocytic primary cilia in the cortex (Fig. 5E). Therefore, with this approach, primary cilia signaling is impaired during development when primary cilia can be detected on astrocytes (Supplemental Fig. 3A–B).

We next imaged large areas of somatosensory cortex of each experimental group at P30, a time point when astrocytes are generally stable and mature [55,56] (Fig. 5F–G), and compared astrocytes from mCherry-only, Arl13 B-GFP, and Arl13 B-T35N-GFP conditions. Partitioning the cortex into upper and lower regions (upper layers defined as 0–799 μm from the pial surface; lower layers defined as 800–1500 μm from the pial surface), Arl13 B-T35N-GFP astrocytes were significantly reduced in upper layers of the cortex and significantly increased in the lower layers (Fig. 5H–I) (Upper layers, n = 4, mCherry = 40.9855 ± 7.746685 %, Arl13 B-GFP = 38.12883 ± 20.1797 %, Arl13 B-T35N-GFP = 10.48414 ± 9.541543 %, p value = 0.0480, 0.0212), (Lower layers, n = 4, mCherry = 59.0145 ± 7.7467 %, Arl13 B-GFP = 61.8 ± 20.1797 %, T35N = 89.51586 ± 9.541543 %, p value (top) = 0.0115 p value (bottom) = 0.048). These differences were unlikely due to general anatomical changes to cortex as cortical thickness remained similar across all conditions (Fig. 5J) (n = 4, mCherry = 1435.54 ± 109.165 μm, Arl13 B-GFP = 1338.34 ± 97.145 μm, Arl13 B-T35N-GFP = 1455.41 ±

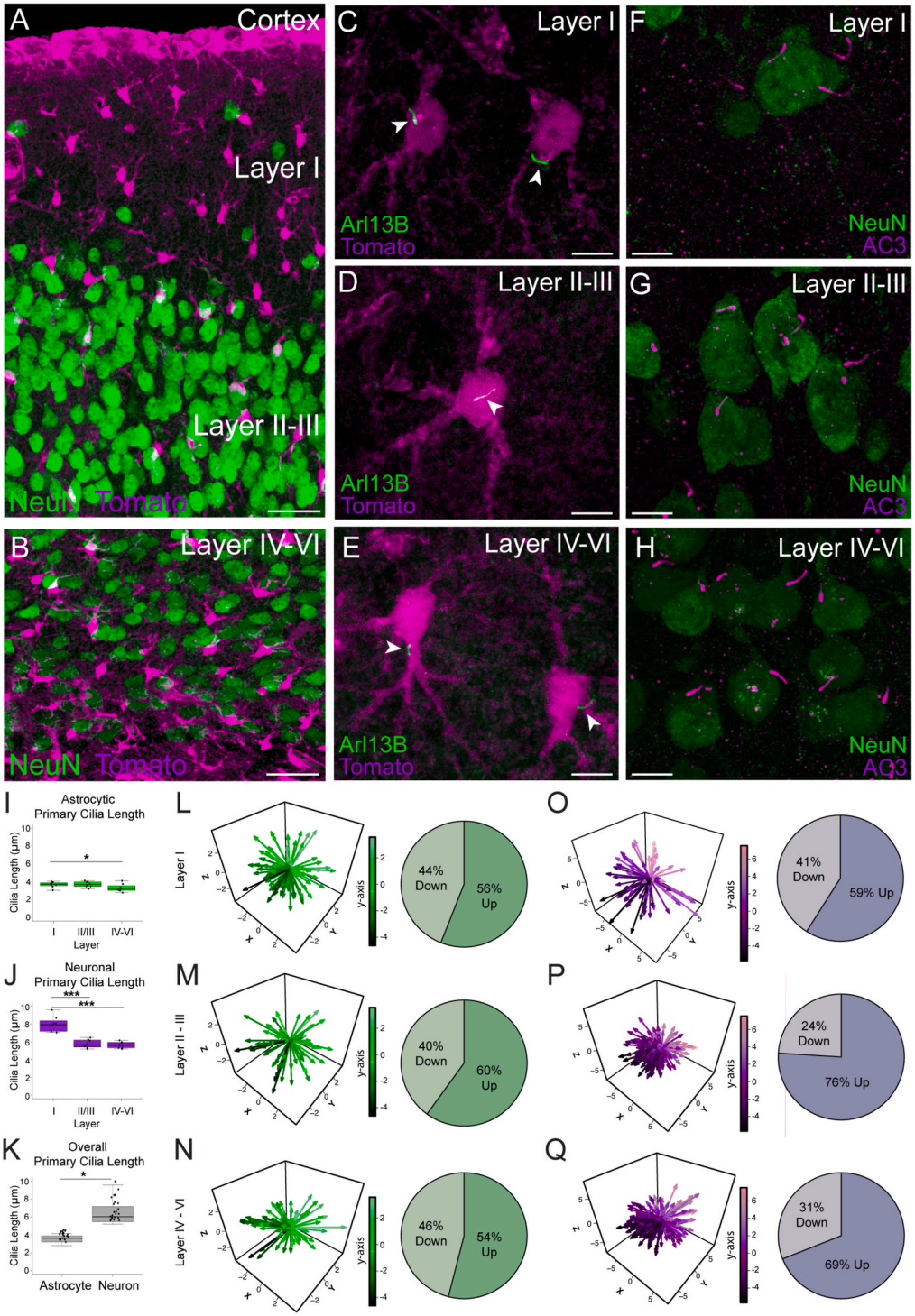

Fig. 3. Astrocytic and neuronal primary cilia in the postnatal day 30 somatosensory cortex. (A) Upper Cortex labeled in Aldh1L1-CreERT2-tdTomato mice with NeuN labeling. Scale bar = 30 µm. (B) Lower cortex of Aldh1L1-CreERT2-tdTomato mice with NeuN labeling. Scale bar = 30 µm. Astrocytic primary cilia labeled with Arl13B in layer I (C), layer II-III (D) and layer IV-VI (E) in the cortex. Scale bar = 5 µm. Neuronal primary cilia labeled with AC3 in layer I (F), layer II-III (G) and layer IV-VI (H) in the cortex. Scale bar = 5 µm. (I) Astrocytic primary cilia length measurements in layer I, layer II-III and layer IV-VI in the cortex (n = 8, layer I = 12–19 cells/animal, layer II - III = 9–23 cells/animal, layer IV-VI = 24–44 cells/animal, 3 sections/animal, p = 0.0623). (J) Neuronal primary cilia length measurements in layer I, layer II-III and layer IV-VI in the cortex (n = 8, layer I = 8–21 cells/animal, layer II - III = 27–49 cells/animal, layer IV-VI = 55–109 cells/animal, 3–6 sections/animal, p (top) = 4.41e-07, p (bottom) = 1.81e-07). (K) Astrocytic and neuronal primary cilia length measurements in all regions of the cortex (n = 8, p = 1.821e-14).

Orientation of astrocyte primary cilia in layer I (L), layer II-III (M) and layer IV-VI (N) (n = 4, layer l = 16–19 cells/animal, layer ll-lll = 9–17 cells/animal, layer lV-Vl = 29–56 cells/animal, 3 sections/animal). Orientation of neuron primary cilia in layer I (O), layer II-III (P) and layer IV-VI (Q) (n = 4, layer l = 10–21 cells/animal, layer ll-lll = 29–37 cells/animal, layer lV-Vl = 11–19 cells/animal, 3–6 sections/animal). Arl13B: ADP-ribosylation factor-like GTPase 13 B; AC3: Adenylate cyclase type III Aldh1L1: Aldehyde dehydrogenase 1 Family Member L1, tdTom: tdTomato, NeuN: Neuronal nuclei. Statical tests used were Student's t-test and ANOVA.

110.611 μm, p value = 0.06815). Examining the average area of individual astrocytes also did not detect significant differences between conditions (Fig. 5K) (n = 4, mCherry = 2493.85 ± 536.38 μm, Arl13 B-GFP = 2735.56 ± 571.23 μm, Arl13 B-T35N-GFP = 2517.50 ± 1033.33 μm p value = 0.8826). Examining an earlier time point of P15 showed a similar result (Supplemental Fig. 3C–F), suggesting that Arl13B GTPase signaling in astrocytic primary cilia helps enable astrocytes to occupy and stabilize in the upper layers of the maturing cortex.

3. Discussion

We applied a combination of light and serial electron microscopy approaches to characterize the structural and organizational properties of astrocytic primary cilia in hippocampal strata and cortical layers. We also quantitatively compared the properties astrocytic primary cilia to the properties of primary cilia in closely juxtaposed neurons. Our results revealed differences between astrocytic and neuronal primary cilia in terms of their molecular composition, length, and orientation. We uncovered subregional differences in both astrocytic and neuronal primary cilia, and revealed some sex-specific differences in primary cilia length. Using a cortical vEM dataset, we further compared the ultrastructural properties of astrocytic and neuronal primary cilia. This demonstrated that astrocytic primary cilia were significantly shorter than neuronal primary cilia, were often deeply buried within a ciliary pocket, and were associated with structures in their local microenvironment including myelinated axons. Disruption of astrocytic primary cilia signaling in developing cortex through expression of a mutant Arl13B protein altered the presence of astrocytes in upper cortical layers when compared to controls. Overall, these findings increase our understanding of the fundamental characteristics of astrocytic primary cilia in the brain and provide deeper insight into their specialized properties that may enable them to effectively respond to cues in their surrounding microenvironment.

An important feature of astrocytes is their ability to actively sense environmental conditions in both the healthy and diseased brain [57,58]. This responsiveness and adaptability is important for astrocyte diversification in the healthy brain and their transition to reactive states upon CNS injury or with disease. Astrocytic diversity in the healthy brain arises through a combination of early progenitor programming and response to environmental cues [28,59,60] leading to transcriptional and structural differences among astrocytes as revealed by single-cell sequencing [61], spatial transcriptomics [46], and structural analysis [47,50]. More recently, Wang et al. [30] used single-cell sequencing with various genetic mouse lines to assess primary cilia transcriptional regulation with both presence and absence of Shh signaling in astrocytes. They observed that astrocytic primary cilia were important for astrocytic diversification with some gene targets being Shh-dependent and others not. Differential signaling of astrocytes in various subregions may contribute to these effects. This is interesting in light of our findings showing the differential orientation of primary cilia for some astrocytic and neuronal populations in hippocampus and cortex and recent findings showing that neuronal primary cilia in the SP of hippocampal CA1 receive axonal input that regulates DNA acetylation [26]. In our analysis, hippocampal astrocytes in the SO showed a preferential orientation toward the SP while astrocytes in other layers did not. In addition, primary cilia of cortical astrocytes did not show an orientation preference. Thus, primary cilia orientation could be especially important for enabling certain hippocampal astrocytic population (i.e SO astrocytes) and neurons (i.e. SP neurons) to make specific contacts with other cells and/or be exposed to spatially restricted environment cues that regulate their molecular and functional properties. In the cortex, astrocytic primary cilia did not show an orientation preference. This contrasts the primary cilia of cortical neurons in layers II-VI which preferentially orient upwards towards the pial surface. This suggests that the mechanisms of growth and stabilization of astrocytic and neuronal primary cilia may be guided by different developmental processes that help orient the primary cilia to different environmental cues and local cellular connectivity.

In our study, we also found differences in primary cilia length that were dependent on sex. Interestingly, these differences were only detected for astrocytic primary cilia and only in particular strata and layers, including SP in hippocampal area CA1 and cortical layers ll-lll. It remains unclear why these differences exist, but it could be related to differences in astrocyte developmental programs between males and females [62]. This could impact development of neurological conditions which have shown sex-related differences such as autism [63], major depressive disorder [64], and Alzheimer's [65] disease in terms of prevalence, symptomology, and onset. As more studies emerge looking at primary cilia signaling in the context of these neurological disorders, it is reasonable to consider the impact of sex differences related to the regulation of primary cilia signaling.

To better resolve the structure and connectivity of astrocytic primary cilia, we utilized a vEM dataset of the adult rat cortex that allowed us to analyze a larger number of astrocytic primary cilia and to perform quantitative geometry comparisons. We found this a useful approach given the complex shape and local connectivity of neurons and astrocytes in the cortex. This approach also enabled us to visualize some aspects of primary cilium ultrastructure including its microtubule arrangement and the structure of the ciliary pocket [23,24]. We observed that astrocytic primary cilia were significantly shorter than neuronal primary cilia, similar to our confocal microscopy results, along with a thinning from base to tip for astrocytic and neuronal primary cilia. An interesting and puzzling feature of astrocyte primary cilia is the prominence of the ciliary pocket which is presumed to limit their exposure to the extracellular environment. Although deep ciliary pockets have been described previously, the variation in this structure in relation to the astrocyte

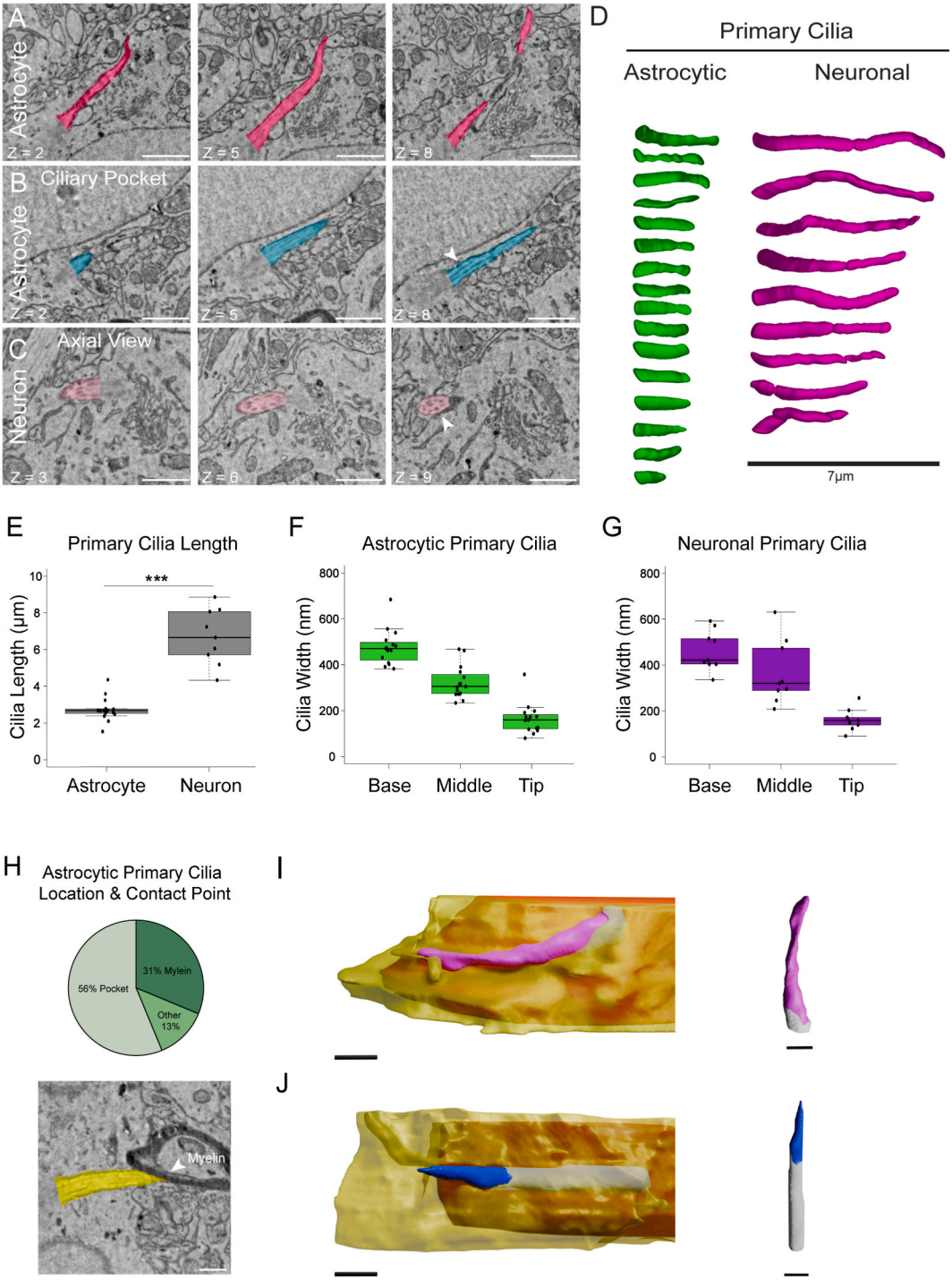

(caption on next page)

Fig. 4. ATUM-SEM of adult rat cortex reveals ultrastructural differences of astrocytic and neuronal primary cilia. (A) An astrocyte primary cilium extending away from the soma. Scale bar = 3 μm. (B) An astrocytic primary cilium contained in a ciliary pocket running along the soma. Scale bar = 3 μm. (C) Neuronal primary cilium sliced in the axial plane. Scale bar = 3 μm. (D) 3D reconstructions of astrocytic and neuronal primary cilia. Scale bar = 7 μm. (E) Comparison of primary cilia length between astrocytes and neurons (astrocytes n = 16; neurons n = 9, p = 2.859e-09). (F) Width measurements of astrocytic primary cilia from base to tip. (G) Width measurements of neuronal primary cilia from base to tip. (H) Astrocytic primary cilia location and contact points within the volume (percentage of observations). The EM micrograph at the bottom shows a single plane of the astrocytic primary cilia in the ATUM-SEM cortical volume (yellow) with primary cilium tip contacting a myelinated axon. Scale bar = 3 μm. (I) 3D reconstruction of an astrocytic primary cilium (magenta) lying along the astrocytic soma with the primary cilia base inside the cell cytoplasm of the soma (yellow). The nucleus is labeled in orange. The isolated reconstruction to the right shows the primary cilium (magenta) with a small region hidden by the somatic membrane (white). Scale bar = 330 nm, 185 nm. (J) 3D reconstruction of an astrocytic primary cilia (blue) embedded deeply within a ciliary pocket with only a small portion of the primary cilium exposed. The nucleus is labeled in orange and the isolated reconstruction to the right shows the primary cilium (blue) with a large region hidden by the somatic membrane (white). Scale bar = 330 nm, 185 nm. ATUM-SEM: Automatic Tape-collecting Ultra-Microtome – Serial Electron Microscopy. Statical tests used were Student's t-test and ANOVA.

membrane and cytoplasm has been under appreciated. Primary cilia are known to use the Shh pathway receptor Smoothened, with it being shuttled to the tip of the primary cilia to promote Gli transcription [30,66]. This poses interesting questions regarding *when*, *why*, and *how* astrocytes choose to expose or hide their primary cilia. Further experiments are required to understand the spatial and temporal dynamics of the astrocytic primary cilium. vEM also enabled us to map the general position of astrocytic primary cilium with respect to other nearby nanostructures. The connectivity of neuronal primary cilia using vEM has been recently reported, along with the discovery of collateral axon synapses on to the CA1 pyramidal cell primary cilia [26]. However, we did not find clear evidence of axonal terminals onto astrocytic primary cilia. Moreover, the majority of astrocytic primary cilia (>50 %) resided in a ciliary pocket with some within deep pockets identified. Some astrocytic primary cilia also made contact with myelinated fibers. The contact between astrocytic primary cilia and myelinated fibers is intriguing given the relationship between astrocytes, oligodendrocytes, and leukodystrophies [67,68].

To better understand how astrocytic primary cilia impact the structure and organization of astrocytes, we introduced a mutant Arl13B T35N protein to perturb primary cilia signaling. This led to fewer astrocytes populating the upper layers of cortex. Interestingly, it was recently showed through single-cell sequencing that astrocytes with altered primary cilia display different transcriptomic alterations between astrocyte subtypes, potentially explaining how our perturbation may more selectively impacting upper layer versus lower layer cortical astrocytes [30]. However, Wang et al. [30] observed a decrease astrocytic area which we did not observe. This may be due to differences in the genetic manipulations performed as well as the timing for loss-of-function. Why there is a selective loss of upper cortical astrocytes, detected as early as P15, following IUE-based astrocytic primary cilia manipulations remains unclear. Since the Arl13B T35N mutation has been shown to disrupt Shh signaling [36], it is possible that this leads to migration defects of immature astrocytes during development [69,70] or alterations in the ability of astrocytes to properly mature which affects their stabilization and retention [71]. Alternatively, loss of Arl13B signaling may impact the ability of astrocytes to undergo local cell proliferation [72,73] in the upper cortical layers perhaps through some superficial or pial-derived signals such as Shh [74]. Lastly, even though the phenotype seems selective to upper cortical astrocytes, cell death at the progenitor or immature astrocyte level could potentially contribute to the alterations observed [75]. Further investigation is needed to test these potential mechanisms.

Important questions remain with respect to astrocytic primary cilia including: (1) What receptors/signaling molecules do astrocytic primary cilia contain and how do they control the structure and transcriptional program of a diverse population of astrocytes, (2) What is the mechanism/purpose of retaining the astrocytic primary cilium in the ciliary pocket and what triggers its extension to increase exposure to environmental cues, and (3) How does the astrocytic primary cilium change when astrocytes become reactive following injury/disease and is their basic function preserved or changed. Further investigation is needed to dissect the function of astrocytic primary cilia and to better understand their role in CNS health and disease.

4. Limitations

There are potential limitations of the study that may impact interpretation of the results. Regarding our results related to light microscopic analysis of primary cilia length and orientation, it is plausible that the markers used for labeling primary cilia (Arl13B and AC3) do not fully label the entire length of the primary cilia and thus underestimate the length of the primary cilia or bias their observed orientation profiles. However, Arl13B and AC3 have been previously used to measure primary cilia in the brain [76]. Our orientation measurements modeled cilia as 3D vectors and did not take into account the curvature along the length of primary cilia. However, based on our observations of ~2000 primary cilia and vEM measurements, the total curvature was small for both neuronal and as well as astrocytic primary cilia. To further validate our results, we directly measured primary cilia length using a vEM dataset. While the dataset was acquired from rat cortex and not mouse cortex, the results reproduced the light microscopy results thus confirming that astrocytic primary cilia are shorter than neuronal primary cilia. We did not observe some of the fine features of primary cilia such as blebbing and vesicles that have been previously described [23,24]. This likely due to the resolution of ATUM-SEM dataset utilized which lacks the same ultrastructural resolution found for other datasets derived from transmission electron microscopy (TEM). However, the large volume of the ATUM-SEM data set was helpful for identifying, segmenting, and analyzing numerous astrocytic and neuronal primary cilia with a level of resolution sufficient to uncover details of the astrocytic primary cilia pocket and interactions within the primary cilia local microenvironment. A final limitation to mention pertains to the IUE gene delivery approach that was utilized. With this method, we were unable to control the number of copies of plasmids each cell received. As a result, some sparse cells

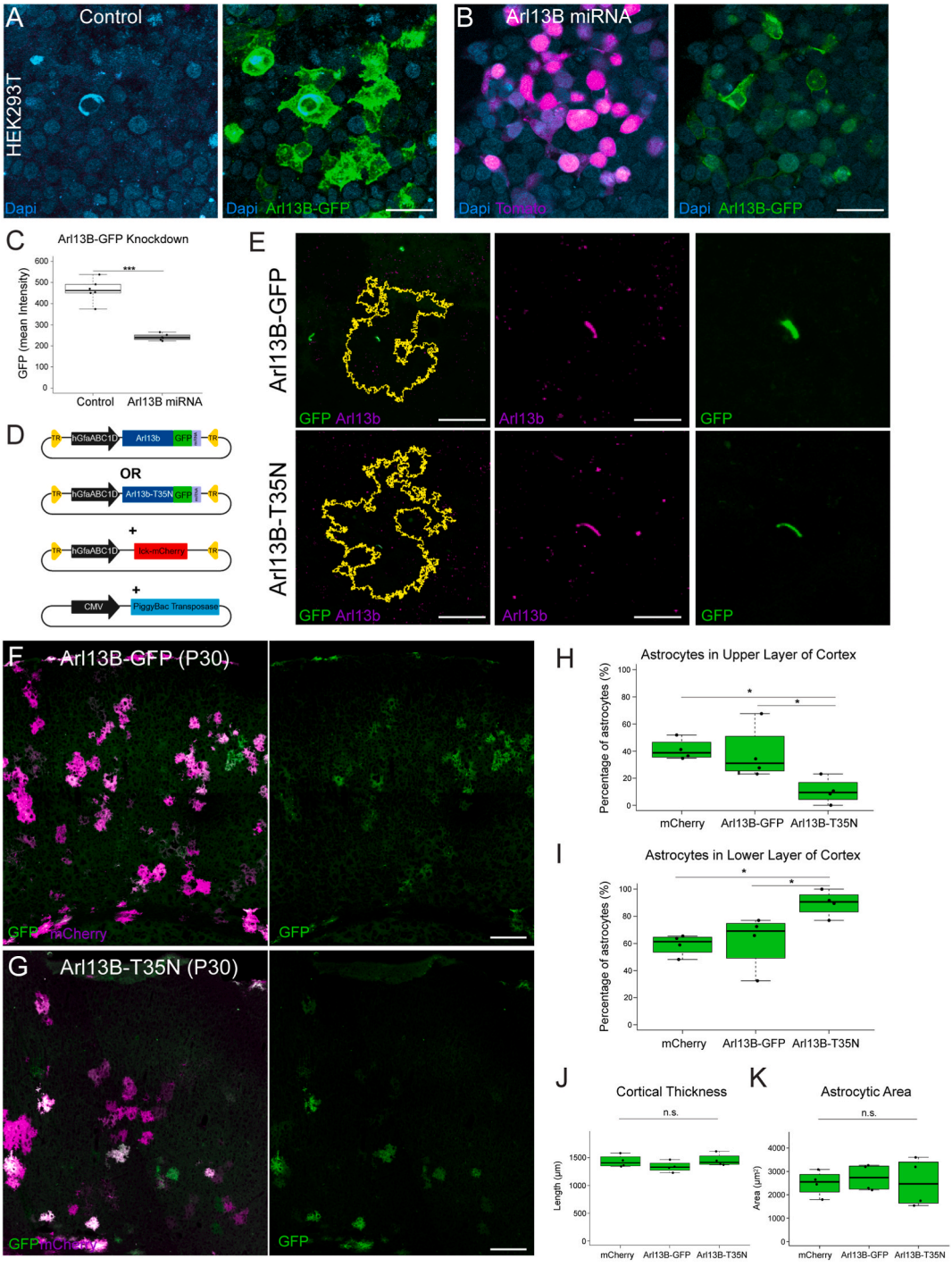

(caption on next page)

Fig. 5. Expression of an Arl13B mutant protein in astrocytes using *in utero* electroporation reduces astrocytes populating upper cortical layers. (A) HEK293T cells transfected with Arl13 B-GFP. Scale = 20 μm. (B) HEK293T cells transfected with Arl13 B-GFP containing a miRNA targeting Arl13B. Co-transfection with a plasmid expressing Tomato to label transfected cells. Scale = 20 μm. (C) Arl13 B-GFP mean intensity in HEK293T cells with or without miRNA (n = 6, p = 2.123e-06). (D) Schematic of *in utero* electroporation (IUE) constructs utilized in the study. (E) High magnification images of Arl13 B-GFP and Arl13 B-T35N expressing astrocytes in cortex with yellow masks representing membrane-targeted mCherry (lck-mCherry) signal expressed by individual astrocytes. Scale bar left = 15 μm, 5 μm. (F) Images of cortical areas of Arl13 B-GFP electroporated mice also expressing lck-mCherry. Scale bar = 30 μm. (G) Image of cortical areas of Arl13 B-T35N electroporated mice expressing lck-mCherry. Scale bar = 30 μm. (H) Percentage of astrocytes found between 800 μm away from corpus callosum to pial surface (n = 4, 15–38 cells per animal, one mosaic/animal, p (top) = 0.0115, p (bottom) = 0.0480). (I) Percentage of astrocytes found between corpus callosum to 800 μm away (n = 4, 15–38 cells per animal, one mosaic/animal, p (top) = 0.0115, p (bottom) = 0.0480). (J) Cortical thickness of mice electroporated with lck-mCherry, Arl13 B-GFP, or Arl13 B-T35N (n = 4, p value = 0.295). (K) Average area of individual astrocytes from mice electroporated with lck-mCherry, Arl13 B-GFP, or Arl13 B-T35N (n = 4, 15–38 cells per animal, p value = 0.8826). Arl13B: ADP-ribosylation factor-like GTPase 13 B, GFP: green florescent protein, miRNA: micro-RNA, tdTom: tdTomato, lck-mCherry: lymphocyte-specific protein tyrosine kinase – mCherry, Dapi: 4′,6-diamidino-2-phenylindole. Statical tests used were Student's t-test and ANOVA.

had Arl13B GFP and Arl13 T35N expression beyond the primary cilia which may lead to additional effects on the cell. However, while the mosaic expression may be a confounding factor, it can also be considered advantageous as some cells also lacked expression of the mutant primary cilia protein and thus could serve as an internal, negative control.

5. Methods

5.1. Animals

Experiments were performed according to the policy set forth by the Canadian Council on Animal Care and the Montreal General Hospital Facility Animal Care Committee (Canada) (AUP 6005) for mouse work or with the guideline of the Institutional Animal Care and Use Committee of the National Institutes for Natural Sciences (Japan) (20A103, 21A009) for rat work. Mice were kept in standard living conditions with access to food and water *ad libitum*. Both males and females were used from the of Aldh1l1-tdTom line containing an inducible Cre allele, directed by the astrocyte-specific aldehyde dehydrogenase family 1, member L1 (Aldh1l1) promoter [41] (Aldh1l1-CreERT2; The Jackson Laboratory) and the floxed-stop Tomato allele [42] (Ai9; The Jackson Laboratory). Recombination of the Tomato allele was induced by injecting mouse pups at postnatal day 1–2 with tamoxifen (Sigma) [28,77].

5.2. Perfusion, fixation, and tissue handling

Mice were transcardially perfused at approximately postnatal day 30 using 4 % paraformaldehyde/0.1M phosphate buffer (PFA). Brains were removed then post fixed in PFA for 24 h before being placed in cryoprotectant solution (30 % sucrose-PBS; Gibco) for approximately another 24h). Brains were then frozen in optimal cutting temperature (OCT) compound (Sakura) and stored at −20 °C. 30 μm brain sections were made using a cryostat (Leica) and kept in PBS at 4 °C until used for immunolabeling.

5.3. Immunolabeling of tissue

Sections were immunolabeled using a free-floating tissue section approach. They were first permeabilized in 1 % Triton X-100/PBS for 15 min in RT, then placed in 10 % normal donkey serum (NDS: Jackson ImmunoResearch) with 0.2 % Triton X-100 (Sigma) blocking solution in PBS for 1h room temperature (RT). After washing sections 3 × 5min in PBS, sections were transferred to a mouse IgG blocking solution (Invitrogen) for 1h at RT. The antibody solution used consisted of 5 % normal donkey serum (NDS) and 0.1 % Triton X-100 in PBS. Sections were incubated in the primary antibody solution overnight at 4 °C. After being washed 3 × 5min in PBS, they were transferred to antibody solution containing secondary antibodies, which were conjugated with Alexa and/or DyLight fluorophores for 1h at RT. Tissue was washed 3 × 5min in PBS, mounted onto slides, and coverslipped using SlowFade Gold (Invitrogen).

The primary antibodies used were the following (See also Table 1) *anti*-ADP-ribosylation factor-like protein 13 B (Arl13B), 1:1500 (mouse monoclonal; Abcam); *anti*-adenylate cyclase III (AC3), 1:4000 (rabbit polyclonal; Invitrogen); anti-neuronal nuclear protein (NeuN), 1:300 (guinea-pig polyclonal; Synaptic Systems); anti-glial fibrillary acidic protein (GFAP), 1:500 (guinea-pig polyclonal; Synaptic Systems); anti-green fluorescent protein (GFP) 1:500 (rat monoclonal; Nacalai). The donkey secondary antibodies used were the following: Dy-light 405 anti-mouse (Jackson ImmunoResearch); Alexa Fluor 488 anti-guinea pig (Jackson ImmunoResearch); Alexa Fluor 647 anti-rabbit (Invitrogen). All secondary antibodies were used at 1:500 dilution. Dapi (Invitrogen) at was used at 1mg/ul

Table 1
Summary of primary antibodies used for immunolabeling.

Target	Manufacturer	Reference Number	Host Species	Type	Dilution Used
Arl13B	Abcam	ab136648	Mouse	Monoclonal	1:1500
AC3	Invitrogen	PA5-35382	Rabbit	Polyclonal	1:4000
NeuN	Synaptic Systems	266 004	Guinea-Pig	Polyclonal	1:300
GFP	Nacalai	044Q4-94	Rat	Monoclonal	1:500

concentration for 15 min at RT after final washes, then washed 3 × 5 min in PBS before being mounted onto slides.

5.4. ATUM-SEM dataset for vEM analysis

A twelve week old Sprague-Dawley male rat was fixed under deep anesthesia with anesthetic of a mixture of medetomidine, midazolam and butorphanol and transcardially perfused with 5 ml of a solution containing 250 mM sucrose, 5 mM $MgCl_2$ in 0.02M phosphate buffer (PB; pH 7.4), followed by 200 ml of 4 % paraformaldehyde, 0.5 % glutaraldehyde containing 0.2 % picric acid in 0.1M PB at room temperature. Brains were left in the body for about 2hrs at room temperature. The frontal cortex was cut into 50 μm thick sections (oblique, horizontal) to preserve apical dendrite of layer 5 pyramidal cell on a vibrating microtome (VT1200S, Leica Microsystems). Tissue sections were stored at −30 °C in cryoprotectant solution (30 % glycerol, 30 % ethylene glycol in 0.04M phosphate-buffered 0.9 % saline [PBS]) until use.

The tissue was processed for EM observation as previously reported [52,78] with slight modification. The following procedures were performed at room temperature unless otherwise stated. The tissue was washed with 0.1M PB followed by washes with 0.1M cacodylate buffer (pH 7.4). The section was then postfixed in 1.5 % potassium ferrocyanide, 2 % osmium tetroxide (OsO_4) in 0.1M cacodylate buffer at 4 °C for 1hr. After the postfixation, the tissue was washed in ultrapure water (Milli-Q® Reference water purification system, Merck Millipore, Burlington, MA), and subsequently stained with 1 % thiocarbohydrazide for 20 min at room temperature, followed by washes with ultrapure water. The section was again postfixed in 2 % OsO_4 for 30min at room temperature and, after washed with ultrapure water, stained overnight at 4 °C with 1 % uranyl acetate. The tissue washed with ultrapure water was processed with modified Walton's *en bloc* lead aspartate staining. Lead aspartate solution was prepared by dissolving 0.066 g of lead nitrate in 10 ml of 0.03M aspartic acid, pH adjusted to 5.0 with 1N potassium hydroxide and kept at 50 °C until dissolved. The tissue was stained with the lead aspartate solution at 50 °C for 2hrs, followed by washes with ultrapure water. The section was then dehydrated in graded dilutions of ethanol and embedded on silicon-coated glass slides in epoxy resin (Durcupan ACM; Sigma-Aldrich, St. Louis, MO). The sample was polymerized at 70 °C for 3 days.

The embedded tissue was serially re-sectioned into 40-nm-thick ultrathin sections and collected using an automated tape collecting ultramicrotome (ATUMtome; Boeckeler Instruments Inc., Tucson, AZ) on a plasma-hydrophilized carbon nanotube-coated polyethylene terephthalate tape (CNT-PET tape) [52]. The following SEM observation was described previously [52]. Briefly, serial ultrathin sections on tape were cut into strips and mounted in order on 4-inch silicon wafers with double-sided adhesive conductive tape. Conductive surface of the CNT-PET tape was grounded to the wafer with copper foil tape. The serial EM images were obtained using a backscattered-electron detector (BSD) of field emission (FE) SEM (Regulus 8240, Hitachi High-Tech Corporation, Tokyo, Japan) with a guide of Auto Capture for Array Tomography (ACAT, Hitachi High-Tech Corporation, Tokyo, Japan). EM images were captured at a resolution of 5.5 × 5.5 nm [2]/pixel in the X and Y directions. We obtained an EM image stack (189 × 202 μm in XY, 1193 sections of 40 nm thickness [totally 47.7 μm in depth]; about 1.6 TB in file size). Tiled images in a single plane were stitched, and serial mosaic images were aligned on TrakEM2 [79] (https://imagej.net/TrakEM2). The 3D EM images were downscaled to a resolution of 10 × 10 nm [2]/pixel in the XY direction. The EM data stack was sent to Zetta.AI (https://zetta.ai) for a fine alignment and an automated dense segmentation.

5.5. Segmentation, reconstruction and EM analysis

TrakEM2 was used for stack alignment and manual segmentation [79]. Astrocytes were identified by clear cytoplasm, small nucleus, and glycogen granules. Neurons were identified by soma with dense organelles, large nucleus, prominent microtubules, and axonal/and dendritic processes. Primary cilia were located near the nucleus, with sometimes a centriole at the base, distinct microtubule structure, and at times the presence of a ciliary pocket. For segmentation of the soma of astrocytes, the cytoplasm was traced, excluding the cell membrane. For segmenting the nuclei, we traced until the boundary of the nuclear envelope. Primary cilia were traced just outside their membrane. Manually labeled nuclei, cytoplasm and associated primary cilia were used to generate 3D reconstructions of the respective structures. We resampled the data from native (10 nm, 10 nm, 40 nm) voxel resolution to isotropic (10 nm,10 nm, 10 nm) spacing. The isotropic labeled images were then used to generate 3D surface meshes using the fast-marching algorithm. The final visualizations were generated and rendered using blender 3.0 (https://www.blender.org/download/releases/3-0/). For measurements, 1D curve skeletons of manually segmented primary cilia were used to estimate the length and thickness of the cilia. The tubular structure of primary cilia allowed us to reduce the segmented structures into 1D skeletal curves using the public implementation of the TEASAR [80] algorithm. from the kimimaro library [81].

5.6. Cell culture

HEK293T cells (RRID:CVCL_0063) were cultured in DMEM (ThermoFisher) supplemented with 10 % fetal bovine serum (Gibco) and 1 % penicillin/streptomycin (100X, Gibco) at 37 °C with 5 % CO_2 maintained in 10 cm dishes (Corning). Cells were seeded at 20 000 on 0.5 μg/ml poly-D-lysine (Gibco) coated glass coverslips (Fisher Scientific) in a 24-well plate (Sarstedt). Cells were transfected with Lipofectamine 3000 (Fisher Scientific) 24hr after seeding and fixed with 4 % PFA 48 h after.

5.7. DNA constructs

To ensure astrocytes and their precursors, which rapidly divide, were sufficiently labeled without diluting the DNA constructs, we

utilized a PiggyBac transposon system that integrates DNA constructs into chromosomal DNA. All DNA constructs were manually cloned into the PiggyBac plasmid vector (SBI Systems Bioscience) under the modified human GFAP promoter, GfaABC1D, using restriction enzyme cloning (New England Biolabs). The following sequences were obtained from Addgene: GfaABC1D (#19974), Lck (#34924), and Arl13B-GFP (#40879). Mutations were induced in Arl13B-GFP to generate Arl13B-T35N construct and then both constructs had silent mutations introduced to prevent binding of the miRNA we inserted in 3' of GFP. miRNAs targeting Arl13B (3 were tested) were generated and manually cloned into a pCAG-Tomato (#83029) for the initial screening. Most effective miRNA sequence (not including loop and reverse compliment) is ATCACATCCGCTTCGCCTAAA, which we used in final DNA construct. The mCherry sequence was originally obtained from Dr. Roger Tsien (UCSD). All DNA was prepared using the endotoxin-free NucleoBond Xtra Maxi EF kit (Clontech).

5.8. *In utero electroporation*

In utero electroporation was carried out as previously described on ICR/CD-1 mouse embryos of embryonic day E15 $\pm$ 1 or E18 $\pm$ 1 to target progenitors in the subventricular zone [54]. Pregnant mice were anaesthetized by isoflurane gas. A 3 mm incision was made at the abdomen to expose the uterine horns. Around 1.5 μl of plasmid solution was microinjected into the right brain ventricle of the E15 $\pm$ 1 embryos or 3 μl of plasmid solution for E18 $\pm$ 1 embryos using a pulled glass pipette connected to a foot pedal-controlled microinjection pump (Harvard Apparatus, Holliston, MA). 0.1 % (w/v) Fast Green dye (Millipore Sigma, Oakville, Ontario) was added to the plasmid solution to help visualize the injection. A pair of 3 mm diameter tweezer-type electrodes (45–0487, Harvard Apparatus) was placed on the embryonic brains with the positive electrode contacting the frontal area. Five 50 ms square electric pulses at 1 Hz were applied with an electroporator (BTX, Holliston, MA). The voltage used depends on the embryonic stages. 35 V was used for E15 $\pm$ 1 embryos while 45 V was used for E18 $\pm$ 1 embryos. After electroporation, embryos were gently placed back into the abdomen. Warm and sterile phosphate-buffered saline (PBS) was added to the abdominal cavity and the incision was sutured. Pregnant mice were returned to their home cage for recovery.

5.9. *Confocal microscopy*

Confocal imaging was done using an FV-1000 laser scanning microscope equipped with a 60$\times$ objective (NA = 1.4) with Fluoview software (Olympus). Z-stacks of ~45 slices were acquired with step size of 0.3 μm. For imaging of *in utero* electroporated brain tissue, Z-stack imaging was performed on a LSM780 laser scanning microscope (Zeiss) equipped with a 20$\times$ objective (NA = 0.8585). Stacks of ~5 slices were acquired with step of 2.0 μm to create large, 5x5 mosaic landscape images.

5.10. *Quantification of primary cilia length and orientation*

To measure primary cilia length, we used the Simple Neurite Tracer [48] (SNT) plugin in ImageJ. 8 animals were quantified (4 males and 4 females) measuring primary cilia lengths from 3 sections per region. Arl13B and AC3 labeled the primary cilia of astrocytes and neurons, respectively. Prior to inputting the images into SNT, we identified the cell bodies of both astrocytes (Tomato-positive) and neurons (NeuN-positive) that were entirely captured in the z-stacks to increase the likelihood that their primary cilia would be fully captured. Once identified, AC3 and Arl13B signals were put into the SNT plugin, which allowed for the primary cilia to be measured all throughout the stack following the set fluorescent channel. The plugin generate the 3D coordinates of the base and tip of the primary cilia, as well as the length measurement (μm). Orientation of the primary cilia was computed by subtracting the 3D coordinates of the start and endpoints, which provided a vector to reflect which direction the primary cilia was pointing in 3D space.

5.11. *Statistics and coding*

Analyses and data visuals were performed using Python and R (R Core Team, 2021). Python packages including tifffile, kimimaro, numpy and R packages include ggplot2, tidyverse, plot3D, and RColorBrewer were used in our analysis. Means comparisons were performed using Student's t-test or ANOVA and 2-Way ANOVA. Statistical significance was set at $p < 0.05$.

CRediT authorship contribution statement

Sylvie C. Lahaie: Writing – review & editing, Writing – original draft, Visualization, Methodology, Investigation, Formal analysis, Data curation, Conceptualization. **Albert HK. Fok:** Writing – review & editing, Writing – original draft, Visualization, Methodology, Investigation, Formal analysis, Data curation, Conceptualization. **Jessica M. Nicholls:** Writing – review & editing, Writing – original draft, Visualization, Methodology, Investigation, Formal analysis, Data curation, Conceptualization. **Hannah Lee:** Writing – review & editing, Writing – original draft, Visualization, Methodology, Investigation, Formal analysis, Data curation, Conceptualization. **Tabish A. Syed:** Writing – review & editing, Writing – original draft, Visualization, Methodology, Investigation, Formal analysis, Conceptualization. **Sabrina Chierzi:** Writing – review & editing, Writing – original draft, Visualization, Methodology, Investigation, Formal analysis, Data curation, Conceptualization. **Sayuri Hatada:** Writing – review & editing, Writing – original draft, Visualization, Methodology, Investigation, Formal analysis, Data curation, Conceptualization. **Naomi Egawa:** Writing – review & editing, Writing – original draft, Visualization, Methodology, Investigation, Formal analysis, Data curation, Conceptualization. **Alex L. Schober:** Writing – review & editing, Writing – original draft, Visualization, Methodology, Investigation, Formal analysis, Data curation,

Conceptualization. **Tak Yi Mayumi Wong:** Writing – review & editing, Writing – original draft, Visualization, Methodology, Investigation, Formal analysis, Data curation, Conceptualization. **Robert Royston:** Writing – review & editing, Writing – original draft, Visualization, Methodology, Investigation, Formal analysis, Data curation, Conceptualization. **Kaleem Siddiqi:** Writing – review & editing, Writing – original draft, Visualization, Supervision, Methodology, Investigation, Formal analysis, Data curation, Conceptualization. **Yoshiyuki Kubota:** Writing – review & editing, Writing – original draft, Visualization, Supervision, Methodology, Investigation, Funding acquisition, Formal analysis, Data curation. **Keith K. Murai:** Writing – review & editing, Writing – original draft, Visualization, Supervision, Methodology, Investigation, Funding acquisition, Formal analysis, Data curation, Conceptualization.

Declaration of competing interest

The authors declare that they have no known competing financial interests or personal relationships that could have appeared to influence the work reported in this paper.

Acknowledgements

This work was supported by the Canadian Institutes of Health Research (PJT148569, 156247 to K.K.M.); the Natural Sciences and Engineering Research Council of Canada (408044–2011 and 69404 to K.K.M.), a Donald S. Wells Distinguished Scientist Award from the Montreal General Hospital (K.K.M), a Fonds de recherche du Québec – Santé (FRQS) Dual Chair in AI and Brain Health award (K.S. and K.K.M), a Brain/MINDS award by AMED JP23dm0207084, JP24wm0625113, JP24wm0625406 (Y.K.), a JST CREST grant JPMJCR21E2 (Y.K.), a JSPS KAKENHI Grant 23H04689, 24H02314 (Y.K.), FRQS fellowships (A.L.S. and T.Y.M.W), a Canadian Neurodevelopmental Research Training (CanNRT) Platform Fellow (S.C.L), an F. S. B. Miller Fellowship (S.C.L) and IPN Internal Student Awards (S.C.L).

ABBREVIATIONS

Abbreviation	Full name
AC3	Adenylyl Cyclase 3
ACAT	Auto Capture for Array Tomography
Aldh1l1	Aldehyde dehydrogenase 1 Family Member L1
ATUM-SEM	Automatic tape-collecting ultra-microtome–serial electron microscopy
Arl13B	ADP-ribosylation factor-like protein 13 B
AUP	Animal utilization protocols
BSD	Backscattered-electron detector
CNS	Central nervous system
CNT-PET	Carbon nanotube-coated polyethylene terephthalate
Dapi	4′,6-diamidino-2-phenylindole
DNA	Deoxyribonucleic acid
DMEM	Dulbecco's modified eagle medium
EM	Electron microscopy
FE	Field emission
GFAP	Glial fibrillary acidic protein
GFP	Green fluorescent protein
Ift88	Intraflagellar transport protein 88
IUE	*In utero* electroporation
Lck	Lymphocyte-specific protein tyrosine kinase
MCR	Melanocortin receptor
miRNA	Micro ribonucleic acid
NDS	Normal donkey serum
NeuN	Neuronal nuclei
OCT	Optimal Cutting Temperature
PB	Phosphate buffer
PBS	Phosphate-buffered saline
PFA	Paraformaldehyde
RT	Room Temperature
Shh	Sonic hedgehog
SLM	Stratum lacunosum moleculare
SO	Stratum oriens
SP	Stratum pyramidale
SR	Stratum radiatum
tdTom	tdTomato
vEM	Volume electron microscopy
WT	Wild type

Appendix A. Supplementary data

Supplementary data to this article can be found online at https://doi.org/10.1016/j.heliyon.2025.e44010.

References

[1] G.J. Pazour, G.B. Witman, The vertebrate primary cilium is a sensory organelle, Curr. Opin. Cell Biol. 15 (2003) 105–110, https://doi.org/10.1016/s0955-0674(02)00012-1.
[2] V. Singla, J.F. Reiter, The primary cilium as the cell's antenna: signaling at a sensory organelle, Science 313 (2006) 629–633, https://doi.org/10.1126/science.1124534.
[3] K.C. Corbit, P. Aanstad, V. Singla, A.R. Norman, D.Y.R. Stainier, J.F. Reiter, Vertebrate smoothened functions at the primary cilium, Nature 437 (2005) 1018–1021, https://doi.org/10.1038/nature04117.
[4] R. Rohatgi, L. Milenkovic, M.P. Scott, Patched1 regulates hedgehog signaling at the primary cilium, Science 317 (2007) 372–376, https://doi.org/10.1126/science.1139740.
[5] N.F. Berbari, A.D. Johnson, J.S. Lewis, C.C. Askwith, K. Mykytyn, Identification of ciliary localization sequences within the third intracellular loop of G protein-coupled receptors, Mol. Biol. Cell 19 (2008) 1540–1547, https://doi.org/10.1091/mbc.e07-09-0942.
[6] J.A. Green, C. Gu, K. Mykytyn, Heteromerization of ciliary G protein-coupled receptors in the mouse brain, PLoS One 7 (2012) e46304, https://doi.org/10.1371/journal.pone.0046304.
[7] M. Brodsky, A.J. Lesiak, A. Croicu, N. Cohenca, J.M. Sullivan, J.F. Neumaier, 5-HT6 receptor blockade regulates primary cilia morphology in striatal neurons, Brain Res. 1660 (2017) 10–19, https://doi.org/10.1016/j.brainres.2017.01.010.
[8] M. Händel, S. Schulz, A. Stanarius, M. Schreff, M. Erdtmann-Vourliotis, H. Schmidt, G. Wolf, V. Höllt, Selective targeting of somatostatin receptor 3 to neuronal cilia, Neuroscience 89 (1999) 909–926, https://doi.org/10.1016/s0306-4522(98)00354-6.
[9] E.A. Nigg, J.W. Raff, Centrioles, centrosomes, and Cilia in health and disease, Cell 139 (2009) 663–678, https://doi.org/10.1016/j.cell.2009.10.036.
[10] E.S. Seeley, M.V. Nachury, The perennial organelle: assembly and disassembly of the primary cilium, J. Cell Sci. 123 (2010) 511–518, https://doi.org/10.1242/jcs.061093.
[11] J.T. Eggenschwiler, K.V. Anderson, Cilia and developmental signaling, Annu. Rev. Cell Dev. Biol. 23 (2007) 345–373, https://doi.org/10.1146/annurev.cellbio.23.090506.123249.
[12] H. Ishikawa, W.F. Marshall, Ciliogenesis: building the cell's antenna, Nat. Rev. Mol. Cell Biol. 12 (2011) 222–234, https://doi.org/10.1038/nrm3085.
[13] I. Izawa, H. Goto, K. Kasahara, M. Inagaki, Current topics of functional links between primary cilia and cell cycle, Cilia 4 (2015) 12, https://doi.org/10.1186/s13630-015-0021-1.
[14] A. Horani, T.W. Ferkol, Understanding primary ciliary dyskinesia and other ciliopathies, J Pediatrics 230 (2021) 15–22.e1, https://doi.org/10.1016/j.jpeds.2020.11.040.
[15] J.E. Siljee, Y. Wang, A.A. Bernard, B.A. Ersoy, S. Zhang, A. Marley, M.V. Zastrow, J.F. Reiter, C. Vaisse, Subcellular localization of MC4R with ADCY3 at neuronal primary cilia underlies a common pathway for genetic predisposition to obesity, Nat. Genet. 50 (2018) 180–185, https://doi.org/10.1038/s41588-017-0020-9.
[16] M. Oya, Y. Miyasaka, Y. Nakamura, M. Tanaka, T. Suganami, T. Mashimo, K. Nakamura, Age-related ciliopathy: obesogenic shortening of melanocortin-4 receptor-bearing neuronal primary cilia, Cell Metab. (2024), https://doi.org/10.1016/j.cmet.2024.02.010.
[17] J.J. Moser, M.J. Fritzler, J.B. Rattner, Ultrastructural characterization of primary cilia in pathologically characterized human glioblastoma multiforme (GBM) tumors, BMC Clin. Pathol. 14 (2014) 40, https://doi.org/10.1186/1472-6890-14-40.
[18] G. Goranci-Buzhala, A. Mariappan, L. Ricci-Vitiani, N. Josipovic, S. Pacioni, M. Gottardo, J. Ptok, H. Schaal, G. Callaini, K. Rajalingam, et al., Cilium induction triggers differentiation of glioma stem cells, Cell Rep. 36 (2021) 109656, https://doi.org/10.1016/j.celrep.2021.109656.
[19] A.G. Vorobyeva, A.J. Saunders, Amyloid-β interrupts canonical sonic hedgehog signaling by distorting primary cilia structure, Cilia 7 (2018) 5, https://doi.org/10.1186/s13630-018-0059-y.
[20] H.S. Dhekne, I. Yanatori, R.C. Gomez, F. Tonelli, F. Diez, B. Schüle, M. Steger, D.R. Alessi, S.R. Pfeffer, A pathway for Parkinson's disease LRRK2 kinase to block primary cilia and sonic hedgehog signaling in the brain, eLife 7 (2018) e40202, https://doi.org/10.7554/elife.40202.
[21] V.T.T. Nguyen, L. Brücker, A.-K. Volz, J.C. Baumgärtner, M. Guilherme, S. dos, F. Valeri, H. May-Simera, K. Endres, Primary cilia structure is prolonged in enteric neurons of 5xFAD alzheimer's disease model mice, Int. J. Mol. Sci. 22 (2021) 13564, https://doi.org/10.3390/ijms222413564.
[22] S.S. Khan, Y. Sobu, H.S. Dhekne, F. Tonelli, K. Berndsen, D.R. Alessi, S.R. Pfeffer, Pathogenic LRRK2 control of primary cilia and Hedgehog signaling in neurons and astrocytes of mouse brain, eLife 10 (2021) e67900, https://doi.org/10.7554/elife.67900.
[23] C.M. Ott, R. Torres, T.-S. Kuan, A. Kuan, J. Buchanan, L. Elabbady, S. Seshamani, A.L. Bodor, F. Collman, D.D. Bock, et al., Ultrastructural differences impact cilia shape and external exposure across cell classes in the visual cortex, Curr. Biol. 34 (2024) 2418–2433.e4, https://doi.org/10.1016/j.cub.2024.04.043.
[24] J.Y. Wu, S.-J. Cho, K. Descant, P.H. Li, A. Shapson-Coe, M. Januszewski, D.R. Berger, C. Meyer, C. Casingal, A. Huda, et al., Mapping of neuronal and glial primary cilia contactome and connectome in the human cerebral cortex, Neuron 112 (2023) 1–15, https://doi.org/10.1016/j.neuron.2023.09.032.
[25] K. Ono, H. Gotoh, T. Nomura, T. Morita, O. Baba, M. Matsumoto, S. Saitoh, N. Ohno, Ultrastructural characteristics of oligodendrocyte precursor cells in the early postnatal mouse optic nerve observed by serial block-face scanning electron microscopy, PLoS One 17 (2022) e0278118, https://doi.org/10.1371/journal.pone.0278118.
[26] S.-H. Sheu, S. Upadhyayula, V. Dupuy, S. Pang, F. Deng, J. Wan, D. Walpita, H.A. Pasolli, J. Houser, S. Sanchez-Martinez, et al., A serotonergic axon-cilium synapse drives nuclear signaling to alter chromatin accessibility, Cell 185 (2022) 3390–3407.e18, https://doi.org/10.1016/j.cell.2022.07.026.
[27] A.D.R. Garcia, R. Petrova, L. Eng, A.L. Joyner, Sonic hedgehog regulates discrete populations of astrocytes in the adult mouse forebrain, J. Neurosci. 30 (2010) 13597–13608, https://doi.org/10.1523/jneurosci.0830-10.2010.
[28] W.T. Farmer, T. Abrahamsson, S. Chierzi, C. Lui, C. Zaelzer, E.V. Jones, B.P. Bally, G.G. Chen, J.-F. Théroux, J. Peng, et al., Neurons diversify astrocytes in the adult brain through sonic hedgehog signaling, Science 351 (2016) 849–854, https://doi.org/10.1126/science.aab3103.
[29] Y. Xie, A.T. Kuan, W. Wang, Z.T. Herbert, O. Mosto, O. Olukoya, M. Adam, S. Vu, M. Kim, D. Tran, et al., Astrocyte-neuron crosstalk through Hedgehog signaling mediates cortical synapse development, Cell Rep. 38 (2022) 110416, https://doi.org/10.1016/j.celrep.2022.110416.
[30] L. Wang, Q. Guo, S. Acharya, X. Zheng, V. Huynh, B. Whitmore, A. Yimit, M. Malhotra, S. Chatterji, N. Rosin, et al., Primary cilia signaling in astrocytes mediates development and regional-specific functional specification, Nat. Neurosci. 27 (2024) 1708–1720, https://doi.org/10.1038/s41593-024-01726-z.
[31] P. Del Río-Hortega, W. Penfield, Cerebral cicatrix-the reaction of neuroglia and microglia to brain wounds, Bull. Johns Hopkins Hosp. 41 (1927) 278–303.
[32] N.A. Muhamad, K. Masutani, S. Furukawa, S. Yuri, M. Toriyama, C. Matsumoto, S. Itoh, Y. Shinagawa, A. Isotani, M. Toriyama, et al., Astrocyte-Specific inhibition of the primary cilium suppresses C3 expression in reactive Astrocyte, Cell. Mol. Neurobiol. 44 (2024) 48, https://doi.org/10.1007/s10571-024-01482-5.
[33] W. Cao, J. Lin, W. Xiang, J. Liu, B. Wang, W. Liao, T. Jiang, Physical exercise-induced astrocytic neuroprotection and cognitive improvement through primary Cilia and mitogen-activated protein kinases pathway in rats with chronic cerebral hypoperfusion, Front. Aging Neurosci. 14 (2022) 866336, https://doi.org/10.3389/fnagi.2022.866336.
[34] O. Ignatenko, S. Malinen, S. Rybas, H. Vihinen, J. Nikkanen, A. Kononov, E.S. Jokitalo, G. Ince-Dunn, A. Suomalainen, Mitochondrial dysfunction compromises ciliary homeostasis in astrocytes, J. Cell Biol. 222 (2022) e202203019, https://doi.org/10.1083/jcb.202203019.

[35] C. Escartin, E. Galea, A. Lakatos, J.P. O'Callaghan, G.C. Petzold, A. Serrano-Pozo, C. Steinhäuser, A. Volterra, G. Carmignoto, A. Agarwal, et al., Reactive astrocyte nomenclature, definitions, and future directions, Nat. Neurosci. 24 (2021) 312–325, https://doi.org/10.1038/s41593-020-00783-4.

[36] L.E. Mariani, M.F. Bijlsma, A.I. Ivanova, S.K. Suciu, R.A. Kahn, T. Caspary, Arl13b regulates Shh signaling from both inside and outside the cilium, Mol. Biol. Cell 27 (2016) 3780–3790, https://doi.org/10.1091/mbc.e16-03-0189.

[37] Z. Sun, A. Amsterdam, G.J. Pazour, D.G. Cole, M.S. Miller, N. Hopkins, A genetic screen in zebrafish identifies cilia genes as a principal cause of cystic kidney, Development 131 (2004) 4085–4093, https://doi.org/10.1242/dev.01240.

[38] G.A. Bishop, N.F. Berbari, J. Lewis, K. Mykytyn, Type III adenylyl cyclase localizes to primary cilia throughout the adult mouse brain, J. Comp. Neurol. 505 (2007) 562–571, https://doi.org/10.1002/cne.21510.

[39] C.E. Larkins, G.D.G. Aviles, M.P. East, R.A. Kahn, T. Caspary, Arl13b regulates ciliogenesis and the dynamic localization of Shh signaling proteins, Mol. Biol. Cell 22 (2011) 4694–4703, https://doi.org/10.1091/mbc.e10-12-0994.

[40] Y. Ou, Y. Ruan, M. Cheng, J.J. Moser, J.B. Rattner, F.A. van der Hoorn, Adenylate cyclase regulates elongation of mammalian primary cilia, Exp. Cell Res. 315 (2009) 2802–2817, https://doi.org/10.1016/j.yexcr.2009.06.028.

[41] R. Srinivasan, T.-Y. Lu, H. Chai, J. Xu, B.S. Huang, P. Golshani, G. Coppola, B.S. Khakh, New transgenic mouse lines for selectively targeting astrocytes and studying calcium signals in Astrocyte processes in situ and in vivo, Neuron 92 (2016) 1181–1195, https://doi.org/10.1016/j.neuron.2016.11.030.

[42] L. Madisen, T.A. Zwingman, S.M. Sunkin, S.W. Oh, H.A. Zariwala, H. Gu, L.L. Ng, R.D. Palmiter, M.J. Hawrylycz, A.R. Jones, et al., A robust and high-throughput Cre reporting and characterization system for the whole mouse brain, Nat. Neurosci. 13 (2010) 133–140, https://doi.org/10.1038/nn.2467.

[43] D.G. Amaral, M.P. Witter, The three-dimensional organization of the hippocampal formation: a review of anatomical data, Neuroscience 31 (1989) 571–591, https://doi.org/10.1016/0306-4522(89)90424-7.

[44] H.M. Duvernoy, The Human Hippocampus, Functional Anatomy, Vascularization and Serial Sections with MRI, 1998, https://doi.org/10.1007/978-3-662-03628-0.

[45] M.W. Jones, T.J. McHugh, Updating hippocampal representations: CA2 joins the circuit, Trends Neurosci. 34 (2011) 526–535, https://doi.org/10.1016/j.tins.2011.07.007.

[46] M.Y. Batiuk, A. Martirosyan, J. Wahis, F. de Vin, C. Marneffe, C. Kusserow, J. Koeppen, J.F. Viana, J.F. Oliveira, T. Voet, et al., Identification of region-specific astrocyte subtypes at single cell resolution, Nat. Commun. 11 (2020) 1220, https://doi.org/10.1038/s41467-019-14198-8.

[47] J.F. Viana, J.L. Machado, D.S. Abreu, A. Veiga, S. Barsanti, G. Tavares, M. Martins, V.M. Sardinha, S. Guerra-Gomes, C. Domingos, et al., Astrocyte structural heterogeneity in the mouse hippocampus, Glia 71 (2023) 1667–1682, https://doi.org/10.1002/glia.24362.

[48] C. Arshadi, U. Günther, M. Eddison, K.I.S. Harrington, T.A. Ferreira, SNT: a unifying toolbox for quantification of neuronal anatomy, Nat. Methods 18 (2021) 374–377, https://doi.org/10.1038/s41592-021-01105-7.

[49] B.S. Khakh, M.V. Sofroniew, Diversity of astrocyte functions and phenotypes in neural circuits, Nat. Neurosci. 18 (2015) 942–952, https://doi.org/10.1038/nn.4043.

[50] D. Lanjakornsiripan, B.-J. Pior, D. Kawaguchi, S. Furutachi, T. Tahara, Y. Katsuyama, Y. Suzuki, Y. Fukazawa, Y. Gotoh, Layer-specific morphological and molecular differences in neocortical astrocytes and their dependence on neuronal layers, Nat. Commun. 9 (2018) 1623, https://doi.org/10.1038/s41467-018-03940-3.

[51] O.A. Bayraktar, T. Bartels, S. Holmqvist, V. Kleshchevnikov, A. Martirosyan, D. Polioudakis, L.B. Haim, A.M.H. Young, M.Y. Batiuk, K. Prakash, et al., Astrocyte layers in the mammalian cerebral cortex revealed by a single-cell in situ transcriptomic map, Nat. Neurosci. 23 (2020) 500–509, https://doi.org/10.1038/s41593-020-0602-1.

[52] Y. Kubota, J. Sohn, S. Hatada, M. Schurr, J. Straehle, A. Gour, R. Neujahr, T. Miki, S. Mikula, Y. Kawaguchi, A carbon nanotube tape for serial-section electron microscopy of brain ultrastructure, Nat. Commun. 9 (2018) 437, https://doi.org/10.1038/s41467-017-02768-7.

[53] Y. Lee, A. Messing, M. Su, M. Brenner, GFAP promoter elements required for region-specific and astrocyte-specific expression, Glia 56 (2008) 481–493, https://doi.org/10.1002/glia.20622.

[54] C.K. Salmon, T.A. Syed, J.B. Kacerovsky, N. Alivodej, A.L. Schober, T.F.W. Sloan, M.T. Pratte, M.P. Rosen, M. Green, A. Chirgwin-Dasgupta, et al., Organizing principles of astrocytic nanoarchitecture in the mouse cerebral cortex, Curr. Biol. 33 (2023) 957–972.e5, https://doi.org/10.1016/j.cub.2023.01.043.

[55] K.T. Baldwin, K.K. Murai, B.S. Khakh, Astrocyte morphology, Trends Cell Biol. 34 (2023) 547–565, https://doi.org/10.1016/j.tcb.2023.09.006.

[56] S. Clavreul, L. Abdeladim, E. Hernández-Garzón, D. Niculescu, J. Durand, S.-H. Ieng, R. Barry, G. Bonvento, E. Beaurepaire, J. Livet, et al., Cortical astrocytes develop in a plastic manner at both clonal and cellular levels, Nat. Commun. 10 (2019) 4884, https://doi.org/10.1038/s41467-019-12791-5.

[57] S.M. Ki, H.S. Jeong, J.E. Lee, Primary Cilia in glial cells: an Oasis in the journey to overcoming neurodegenerative diseases, Front Neurosci-switz 15 (2021) 736888, https://doi.org/10.3389/fnins.2021.736888.

[58] R. Ma, N.A. Kutchy, L. Chen, D.D. Meigs, G. Hu, Primary cilia and ciliary signaling pathways in aging and age-related brain disorders, Neurobiol. Dis. 163 (2021) 105607, https://doi.org/10.1016/j.nbd.2021.105607.

[59] L.B. Haim, D.H. Rowitch, Functional diversity of astrocytes in neural circuit regulation, Nat. Rev. Neurosci. 18 (2017) 31–41, https://doi.org/10.1038/nrn.2016.159.

[60] W.T. Farmer, K. Murai, Resolving astrocyte heterogeneity in the CNS, Front. Cell. Neurosci. 11 (2017) 300, https://doi.org/10.3389/fncel.2017.00300.

[61] P.W. Frazel, D. Labib, T. Fisher, R. Brosh, N. Pirianian, A. Marchildon, J.D. Boeke, V. Fossati, S.A. Liddelow, Longitudinal scRNA-seq analysis in mouse and human informs optimization of rapid mouse astrocyte differentiation protocols, Nat. Neurosci. (2023) 1–13, https://doi.org/10.1038/s41593-023-01424-2.

[62] G.M. Rurak, S. Simard, M. Freitas-Andrade, B. Lacoste, F. Charih, A.V. Geel, J. Stead, B. Woodside, J.R. Green, G. Coppola, et al., Sex differences in developmental patterns of neocortical astroglia: a mouse translatome database, Cell Rep. 38 (2022) 110310, https://doi.org/10.1016/j.celrep.2022.110310.

[63] T. May, I. Adesina, J. McGillivray, N.J. Rinehart, Sex differences in neurodevelopmental disorders, Curr. Opin. Neurol. 32 (2019) 622–626, https://doi.org/10.1097/wco.0000000000000714.

[64] S. Mohammadi, H. Seyedmirzaei, M.A. Salehi, A. Jahanshahi, S.S. Zakavi, F.D. Firouzabadi, D.M. Yousem, Brain-based sex differences in depression: a systematic review of neuroimaging studies, Brain Imaging Behav 17 (2023) 541–569, https://doi.org/10.1007/s11682-023-00772-8.

[65] J.E. Young, M. Wu, H.C. Hunsberger, Editorial: sex and gender differences in neurodegenerative diseases, Front. Neurosci. 17 (2023) 1175674, https://doi.org/10.3389/fnins.2023.1175674.

[66] F. Bangs, K.V. Anderson, Primary Cilia and Mammalian hedgehog signaling, Cold Spring Harb. Perspect. Biol. 9 (2017) a028175, https://doi.org/10.1101/cshperspect.a028175.

[67] M. Bugiani, M. Breur, Leukodystrophies due to astroyctic dysfunction, Brain Pathol. 28 (2018) 369–371, https://doi.org/10.1111/bpa.12607.

[68] L.M. Garcia, J.L. Hacker, S. Sase, L. Adang, A. Almad, Glial cells in the driver seat of leukodystrophy pathogenesis, Neurobiol. Dis. 146 (2020) 105087, https://doi.org/10.1016/j.nbd.2020.105087.

[69] F. Memi, N. Zecevic, N. Radonjić, Multiple roles of Sonic Hedgehog in the developing human cortex are suggested by its widespread distribution, Brain Struct. Funct. 223 (2018) 2361–2375, https://doi.org/10.1007/s00429-018-1621-5.

[70] K.M. Markey, J.C. Saunders, J. Smuts, C.R. von Reyn, A.D.R. Garcia, Astrocyte development—More questions than answers, Front. Cell Dev. Biol. 11 (2023) 1063843, https://doi.org/10.3389/fcell.2023.1063843.

[71] E.C. Gingrich, K. Case, A.D.R. Garcia, A subpopulation of astrocyte progenitors defined by Sonic hedgehog signaling, Neural Dev. 17 (2022) 2, https://doi.org/10.1186/s13064-021-00158-w.

[72] M. Komada, Sonic hedgehog signaling coordinates the proliferation and differentiation of neural stem/progenitor cells by regulating cell cycle kinetics during development of the neocortex, Congenit. Anom. 52 (2012) 72–77, https://doi.org/10.1111/j.1741-4520.2012.00368.x.

[73] W.-P. Ge, A. Miyawaki, F.H. Gage, Y.N. Jan, L.Y. Jan, Local generation of glia is a major astrocyte source in postnatal cortex, Nature 484 (2012) 376–380, https://doi.org/10.1038/nature10959.

[74] O.R. Yabut, S.J. Pleasure, Sonic hedgehog signaling rises to the surface: emerging roles in neocortical development, Brain Plast. 3 (2018) 119–128, https://doi.org/10.3233/bpl-180064.

[75] S.C. Ahlgren, V. Thakur, M. Bronner-Fraser, Sonic hedgehog rescues cranial neural crest from cell death induced by ethanol exposure, Proc. Natl. Acad. Sci. 99 (2002) 10476–10481, https://doi.org/10.1073/pnas.162356199.
[76] É. Sipos, S. Komoly, P. Ács, Quantitative Comparison of Primary Cilia Marker Expression and Length in the Mouse Brain, J. Mol. Neurosci. 64 (2018) 397–409, https://doi.org/10.1007/s12031-018-1036-z.
[77] S. Chierzi, J.B. Kacerovsky, A.H. Fok, S. Lahaie, A. Shibi-Rosen, W.T. Farmer, K.K. Murai, Astrocytes transplanted during early postnatal development integrate, mature, and survive long-term in mouse cortex, J. Neurosci. 43 (2023), https://doi.org/10.1523/jneurosci.0544-22.2023. JN-RM-0544-22.
[78] Y. Hua, P. Laserstein, M. Helmstaedter, Large-volume en-bloc staining for electron microscopy-based connectomics, Nat. Commun. 6 (2015) 7923, https://doi.org/10.1038/ncomms8923.
[79] A. Cardona, S. Saalfeld, J. Schindelin, I. Arganda-Carreras, S. Preibisch, M. Longair, P. Tomancak, V. Hartenstein, R.J. Douglas, TrakEM2 software for neural circuit reconstruction, PLoS One 7 (2012) e38011, https://doi.org/10.1371/journal.pone.0038011.
[80] M. Sato, I. Bitter, M. Bender, A. Kaufan, M. Nakajima, Teasar: tree-structure extraction algorithm for accurate and robust skeletons, Proceedings the Eighth Pacific Conference on Computer Graphics and Applications (2000) 281–449, https://doi.org/10.1109/PCCGA.2000.883951.
[81] W. Silversmith, J.A. Bae, P.H. Li, A.M. Wilson, Kimimaro: Skeletonize Densely Labeled 3d Image Segmentations, Zenodo, 2021, https://doi.org/10.5281/zenodo.5539912.